Cs in a cryogenic matrix, towards a measurement of the electron electric dipole moment

Masterarbeit in Physik

Von Sebastian Lahs

angefertigt im Laboratoire Aimé Cotton

vorgelegt der Mathematisch-Naturwissenschaftlichen Fakultät der Universität Bonn

1. Gutachter : Prof. Daniel Comparat

2. Gutachter : Prof. Simon Stellmer

I hereby declare that the work presented here was formulated by myself and that no sources or tools other than those cited were used.

Orsay, 31.08.2022

Abstract. To explain the open questions in the fundaments of physics, new theories that reach beyond the standard model are needed. A great number of these indirectly predict electric dipole moments (EDM) of fundamental particles in ranges that are just within reach for modern atomic and molecular physics experiments. While measurements in atomic and molecular beams provided the most successful null measurements of the electron EDM over the past decades, only quite recently did the method of matrix isolation spectroscopy arise. It has the potential advantage of performing spectroscopy on un- precedented numbers of atoms/molecules at once. In this thesis, first tests toward such a measurement inside of a cryogenic matrix are performed. Namely cesium and rubidium were implanted in argon ice. The observed absorption and fluorescence spectra will be presented here. This will be accompanied by a discussion on possible systematics due to magnetoelectric mixings. Finally, the possibility of using this technique for searches of the hypothetical axion particles and for a measurement of the nuclear anapole moment will be discussed.

Contents

1 Introduction

Even though the standard model of particle physics (SM) has been tested time and time again to ever-increasing precision, its numerical predictions still seem to perfectly hold up. On the other side, there are many phenomena remaining, that the standard model is fully unable to explain (dark matter, neutrino oscillations, matter-antimatter asymmetry after the big bang, hierarchy problems, cosmic inflation, ...). To provide insight into these, new theories beyond the SM are needed. A great variety of these naturally include new sources of violation of charge conjugation-parity (CP) -symmetry.
In section 2, I will explain how this symmetry breaking would express in a detectable electric dipole moment of electrons, and in a further step, in atoms. To detect this electron EDM (eEDM), a variety of measurement schemes have been proposed over the years. In the here presented project, which is done as part of the EDMMA[1] collaboration, studies for a relatively new measurement scheme are performed. Its aim is to perform spectroscopy (or magnetometry) on a large number of atoms, much more than would be achievable inside an atomic beam or a gas cell. At the same time, the atoms should be as undisturbed as possible to achieve long decoherence times (see sec. 3). To bring these two requirements together, the atoms are doped into a host matrix made from noble-gas atoms[2] at cryogenic temperatures. The noble-gas ice provides a transparent, weakly interacting structure, which is able to hold large quantities of single guest atoms in place.

Still, the guest atoms will experience some disturbances due to interactions with the host matrix. Understanding these is one of the main challenges toward a successful eEDM experiment in this scheme.
Therefore in sec. 4, I will discuss one of these interactions, the magnetoelectric effect. I show how this effect can lead to almost insuppressible background signals in asymmetric crystal environments. I however will also provide ways to escape these.

In the experiment presented in this thesis, argon (Ar) was used to form the host matrix. Its advantages lie in its easy availability and the fact that Ar gas is mostly made of a single isotope with vanishing nuclear angular momentum. As dopants, the alkali atoms cesium (Cs) and rubidium (Rb) were used. These heavy atoms with an unpaired electron possess advantageous properties for eEDM searches[1].

In sec. 6.1 I will present absorption spectra of Cs in Ar and Rb in Ar and analyze how their structure could be explained. This is accompanied by fluorescence measurements on Rb in Ar (sec. 6.2) and studies of its permanent and temporary bleaching effects (sec. 6.3). These should be helpful for future measurement of fluorescence of Cs in Ar.

The thesis concludes with two theoretical investigations into other measurements that could be performed with matrix isolation spectroscopy as well. Namely, it will be shown how eEDM measurements provide sensitivity to axions, a proposed particle species, that could make up dark matter (sec. 8). I will provide an argument on why eEDM experi-

[1] acronym for the ANR founded project **EDM** in **MA**trix

[2] It is also possible to use strongly bound molecules like N_2 or parahydrogen.

ments should generally aim at measuring bounds on axions as well.
Further I will summarize a measurement scheme to determine the nuclear anapole moments (NAM) of guest atoms inside matrices. I will present some thoughts on how to measure this effect, which is predicted in the standard model but only poorly probed yet.

2 Electric Dipole Moment of the electron

In classical electrodynamics, as well as in quantum mechanics, the electron is just a point charge. As such, its electrostatic potential is completely described by an electric monopole. Extending the theoretical model to quantum electrodynamics (QED), the electron interacts with the surrounding vacuum. This way the electron gets 'dressed' in a spherical cloud of Fermion-Antifermion pairs that screens off parts of its charge. Even this does not give rise to higher multipoles as the effective charge distribution is perfectly spherical. Only if the whole standard model of particle physics (SM) with the inclusion of the weak and the strong force is respected, theory predicts that the interaction with the SM vacuum gives rise to an electric dipole moment of the electron (eEDM) of magnitude $d_e \sim 10^{-39}\, e\,\mathrm{cm}$ [2][3]. The existence of a dipole moment means that the electric (far-) field around an electron is not spherical anymore but instead slightly deformed (see fig. 1).

2.1 Symmetry breaking properties of the EDM

To understand the minuscule size of this contribution to the electron's potential, it helps to consider the symmetry properties of EDMs together with the symmetry (and violations of these) in the SM. The symmetries under consideration here, are charge conjugation C, parity P, and time reversal T. Charge conjugation C is an operation that reverses the sign of all charges[4]. Parity P on the other hand reverses the sign of all spatial coordinates, while time reversal T reverses the sign in front of the temporal one. As being a vector

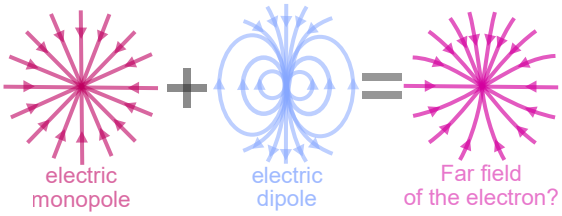

Figure 1: Illustration of how the electrostatic potential of a charged particle with permanent electric dipole moment would look like.

[3] An often cited calculation for the eEDM in the SM gives $d_e \sim 10^{-44}\, e\,\mathrm{cm}$ [3]. In [2] it was however noticed that the long-distance hadronic contributions play a much larger role than previously thought.

[4] $\hat{=}$ transforming particles into their respective antiparticles.

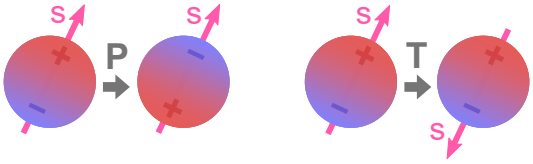

Figure 2: Illustration of how a particle with spin s and permanent electric dipole moment transforms under parity P and time reversal T.

in real space, the electric dipole moment $\boldsymbol{d}_e$ changes sign under P, while the spin $\boldsymbol{s}$ as being a vector in the complex spin-vector-space stays invariant under such a transform. The case is exactly reversed under T transform. In fig 2, this behavior is visualized. A Fermion with a permanent EDM, therefore, breaks P and T symmetry.
The electromagnetic and the strong interaction are symmetric under the application of C, CP, and T. The weak interaction, on the other hand, violates P symmetry maximally and additionally possesses small CP violation in its mixing of quark flavors[5]. All interactions in the SM conserve the combined symmetry of CPT. This implies that a CP violation automatically corresponds to a T violation of the same magnitude. These considerations directly imply that the only interaction in the standard model able to induce an EDM is the weak interaction between quarks. Especially in the case of electrons, the EDM value arising from this contribution is only very small. A non-zero electron EDM (eEDM) only emerges if all Feynman diagrams up to 4th loop order are summed [3].

2.2 eEDM in theories beyond the standard model

Current eEDM measurements are not aiming at measuring the value predicted in the standard model as their sensitivity is still orders of magnitude too low[6]. Instead, they are looking for larger values for d_e, that are predicted in numerous theoretical models for new physics beyond the standard model [6][7]. These theories introduce new particles and interactions to provide solutions to open questions in the fundaments of physics. For example, in the standard model, there are not enough sources of CP violation to explain how the universe was able to evolve into a state with more matter than antimatter [8].
Introducing new forms of CP violation into models, even at high energies, leads in most cases to an increase of the expected value of d_e [6]. Even if a model introduces interactions with no new CP violation, the value of d_e could still be enhanced due to increased couplings of the electron to the diagrams that violate CP symmetry in the SM.

[5]The CP violation expresses as complex phases in the Cabibbo-Kobayashi-Maskawa-Matrix, that describes how W-bosons interact with quarks [4].

[6]Todays most sensitive measurement, done in the ACME II experiment, reports a value of $d_e = (4.3{\pm}3.1_{\text{stat}}{\pm}2.6_{\text{syst}}){\times}10^{-30}\,e$ cm [5].

This all makes EDM measurements a powerful tool for probing proposed theories in particle physics beyond the standard model. For example, some of the particles predicted by simple versions of supersymmetry would couple to electrons in one-loop diagrams. This however would produce values of the eEDM that are orders of magnitude larger than current experiments. This way eEDM measurements can already rule out a set of supersymmetric theories while providing valuable constraints on other more elaborate ones [9].

2.3 eEDM in atoms

In the following, the theory of how eEDMs emerge and in which way they express in atoms is presented. This will be done with the aim to understand which properties a system requires to provide the highest possible sensitivity to the value of the eEDM, d_e.

2.3.1 Quantum field theoretical origins of the eEDM

The matrix element for the most general electromagnetic current can be constructed from writing all the possible combinations of Lorentz invariant vector currents involving γ^μ,γ^5 and q^μ [10][11]:

$$\left\langle \psi(p') \left| J_\mu^{em} \right| \psi(p) \right\rangle \tag{1}$$
$$= \bar{u}(p') \left(F_1\left(q^2\right)\gamma^\mu - i\frac{F_2\left(q^2\right)}{2M}\sigma^{\mu\nu}q_\nu + \frac{F_{\mathbf{a}(q^2)}}{M^2}\left(\gamma^\nu q_\nu q^\mu - q^2\gamma^\mu\right)\gamma_5 - i\frac{F_d\left(q^2\right)}{M}\sigma^{\mu\nu}q_\nu\gamma_5 \right) u(p)$$

p_μ and p'_μ	initial and final four-momenta
q_μ	$p'_\mu - p_\mu$
$\lvert\psi(p)\rangle$	initial state of the electron field
$\langle\psi(p')\rvert$	final state of the electron field
J_μ^{em}	electromagnetic four-current
$\bar{u}(p')$ and $u(p)$	Dirac spinor fields
γ_μ	Dirac gamma matrix
γ_5	$i\gamma_0\gamma_1\gamma_2\gamma_3$
$\sigma_{\mu\nu}$	$\frac{i}{2}\left[\gamma_\mu,\gamma_\nu\right]$
m	electron mass
$\bar{u}(p')u(p)$	scalar coupling
$\bar{u}(p')\gamma^5u(p)$	pseudo-scalar coupling
$\bar{u}(p')\gamma^\mu u(p)$	vector coupling
$\bar{u}(p')\gamma^m u\gamma^5 u(p)$	pseudo(axial)-vector coupling
$\bar{u}(p')\sigma^{\mu\nu}u(p)$	tensor coupling
$\bar{u}(p')\sigma^{\mu\nu}\gamma^5u(p)$	pseudo-tensor coupling

Table 1: Legend for eq. 1.

The meaning of the different symbols can be found in table 1 [7].
The F_i in this equation are called form factors. In the limit of low energy transfers ($q^2 \to 0$), $F_1(0)$ is the charge, $F_2(0)$ the anomalous magnetic moment $\frac{g-2}{2}$, $F_{\mathbf{a}(0)}$ the anapole moment $\mathbf{a}$(see sec. 9), and $F_d(0)$ the electric dipole moment d. Often in discussions on the Dirac Fermion form factors, the terms with F_d and $F_\mathbf{a}$ are left out [11][12]. This is due to their symmetry-breaking behavior. $F_\mathbf{a}$ is odd under parity transform while F_d is odd under both parity and time-reversal [10]. Breaking of these symmetries is not allowed in QED, but with the inclusion of the weak force, they become possible. Respecting the effects of the weak interaction, one gets back the effective QED current (1) with non-zero form factors F_d and $F_\mathbf{a}$.

2.3.2 EDM interactions

Coupling the part of the current from (1) that corresponds to the EDM to the electromagnetic field tensor $F^{\mu\nu}$, yields the following Lagrangian:

$$\mathcal{L}_\mathrm{d} = -i\frac{d}{2}\,\bar{\psi}(\boldsymbol{x})\sigma^{\mu\nu}\gamma_5\psi(\boldsymbol{x})F_{\mu\nu}(\boldsymbol{x})$$

This expression can be rewritten into an interaction with external electric and magnetic fields $\boldsymbol{E}$ and $\boldsymbol{B}$ [9]:

$$\mathcal{L}_\mathrm{d} = d\bar{\psi}(\boldsymbol{x})\left[2\,\boldsymbol{S}\cdot\boldsymbol{E} + i\boldsymbol{\alpha}\cdot\boldsymbol{B}\right]\psi(\boldsymbol{x}) \tag{2}$$

Here $\boldsymbol{S}$ is the relativistic spin operator and $\boldsymbol{\alpha}$ are Dirac matrices. In Dirac convention they can be represented as the following 4x4 matrices:

$$\boldsymbol{S}_i = \frac{1}{2}\begin{pmatrix}\boldsymbol{\sigma}_i & 0\\ 0 & \boldsymbol{\sigma}_i\end{pmatrix},\quad \boldsymbol{\alpha}_i = \gamma^0\gamma^i = \begin{pmatrix}0 & \boldsymbol{\sigma}_i\\ \boldsymbol{\sigma}_i & 0\end{pmatrix}$$

with the Pauli matrices $\boldsymbol{\sigma}_i$.
Using $\bar{\psi}(\boldsymbol{x}) = \psi^\dagger(\boldsymbol{x})\gamma_0$, (2) one can derive the corresponding one-particle Hamiltonian trough a Legendre transformation:

$$H_\mathrm{d} = -d\left[2\,\gamma_0\boldsymbol{S}\cdot\boldsymbol{E} + i\gamma_0\boldsymbol{\alpha}\cdot\boldsymbol{B}\right] \tag{3}$$

Now, for simplicity, a zero magnetic field is assumed[8]. The Hamiltonian (3) can be split up into a classical and a relativistic part:

$$\begin{aligned} H_\mathrm{d} &= H_\mathrm{d}^\mathrm{clas} + H_\mathrm{d}^\mathrm{rel} = \left[-2d\,\boldsymbol{S}\cdot\boldsymbol{E}\right]^\mathrm{clas} + \left[-2d\,(\gamma_0 - \mathbb{1})\boldsymbol{S}\cdot\boldsymbol{E}\right]^\mathrm{rel}\\ &= \begin{pmatrix}-2d\,\boldsymbol{S}\cdot\boldsymbol{E} & 0\\ 0 & -2d\,\boldsymbol{S}\cdot\boldsymbol{E}\end{pmatrix} + \begin{pmatrix}0 & 0\\ 0 & 4d_e\,\boldsymbol{S}\cdot\boldsymbol{E}\end{pmatrix} \end{aligned} \tag{4}$$

In this Hamiltonian upper and lower components of the Dirac spinor $\psi = (\psi_U\,,\,\psi_L)^\intercal$ do not get mixed. In the non-relativistic limit (e.g. analogous to chapter 5.3.5.3 of [13]), only the upper components ψ_U survive. They correspond to the usual Pauli spinor. The term $H_\mathrm{d}^\mathrm{rel}$ does not contribute in this limit and is therefore called 'relativistic part'.

[7] For simplicity, the derivation in this section is done in natural units: $\hbar = c = 4\pi\varepsilon_0 = 1$

[8] If carried on further it would also turn out that the term proportional to B is negligible [9].

2.3.3 Schiff's theorem

One can show that the term $H_{\mathrm{d}}^{\mathrm{rel}}$ from (4) is not able to create an energy shift [9]. This fact is known as Schiff's theorem. It can be demonstrated as follows:

Let H_{Atom} be the Dirac Hamiltonian of an electron (without EDM) inside an atom, surrounded by an external electric potential Φ_{e}:

$$H_{\mathrm{Atom}} = \boldsymbol{\alpha} \cdot \boldsymbol{p} + m\gamma^0 - e\Phi, \quad H_{\mathrm{Atom}}|\psi\rangle = \mathcal{E}_\psi|\psi\rangle \tag{5}$$

With Φ Being the total electric potential inside the atom[9]. Now one can write:

$$H_{\mathrm{d}}^{\mathrm{clas}} = -2d_e\, \boldsymbol{S} \cdot \boldsymbol{E} = \frac{2d}{e} \boldsymbol{S} \cdot \nabla e\Phi = \frac{2id_e}{e}[\boldsymbol{S} \cdot \boldsymbol{p}, e\Phi] = -\frac{2id_e}{e}\left[\boldsymbol{S} \cdot \boldsymbol{p}, \left(H_{\mathrm{Atom}} - \boldsymbol{\alpha} \cdot \boldsymbol{p} - m\gamma^0\right)\right]$$

The commutator with the sum can be split up into a sum of three simpler ones. $[\boldsymbol{S}, \boldsymbol{\alpha}] = 0$ and $[\boldsymbol{S}, \gamma^0] = 0$. So only $\frac{2id_e}{e}[\boldsymbol{S} \cdot \boldsymbol{p}, H_{\mathrm{Atom}}]$ survives. Therefore the energy shift due to the classical part of the EDM Hamiltonian is given by[10]:

$$\Delta\mathcal{E} = \left\langle \psi \left| H_{\mathrm{d}}^{\mathrm{clas}} \right| \psi \right\rangle = -\frac{2id_e}{e}\langle\psi|[\boldsymbol{S} \cdot \boldsymbol{p}, H_{\mathrm{Atom}}]|\psi\rangle = -\frac{2id_e}{e}\langle\psi|[\boldsymbol{S} \cdot \boldsymbol{p}, \mathcal{E}_\psi]|\psi\rangle = 0$$

Therefore there is no energy shift from the EDM in the non-relativistic limit. This observation was first made by L. I. Schiff in 1963 [14]. In simple terms, it states that the expectation value of the internal electric field inside an atom will cancel out any externally applied electric field, due to electron cloud reorganization.

2.3.4 Sandars solution to the Schiffs theorem

Two years after Schiff's publication, P.G.H Sandars discovered that this issue resolves when the relativistic behavior of the electrons is taken into account[15][11]. Even though the average electric field inside the atom vanishes, the value of the eEDM d_e will not be constant over the volume of its orbital but will instead change due to relativistic length contraction [9]. Therefore the eEDM is able to induce an energy shift despite Schiff's theorem:

From the vanishing of $H_{\mathrm{d}}^{\mathrm{clas}}$ shown in the previous section, it follows:

$$\Delta\mathcal{E} = \langle\psi|H_{\mathrm{d}}|\psi\rangle = \langle\psi|H_{\mathrm{d}}^{\mathrm{rel}}|\psi\rangle = \langle\psi| \begin{pmatrix} 0 & 0 \\ 0 & 4d_e\, \boldsymbol{S} \cdot \boldsymbol{E} \end{pmatrix} |\psi\rangle = \boxed{4d_e\langle\psi_L|\boldsymbol{S} \cdot \boldsymbol{E}|\psi_L\rangle} \tag{6}$$

Calculating this expectation value will directly yield the energy shift observable in an eEDM experiment.
Because this effect is highly relativistic, it is necessary to use heavy atoms with fast-moving electrons to achieve the highest possible energy shift. It scales approximately with the cube of the nuclear charge [7].

[9] With $\Phi_{\mathrm{e}} \to 0$,Φ becomes the coulomb potential.

[10] The Eigenfunctions of the whole system $|\psi\rangle$ are pretty much identical with the Eigenfunctions of H_{Atom}. The only additional contribution is given by perturbation through the EDM term. But because the next order perturbation would already scale with d^2, it clearly can be neglected.

[11] Also considering the nucleus finite size leads to nonzero correction to Schiff's theorem [16].

2.3.5 Energy shift in parity eigenstates

It can be shown that in a system of defined parity, the previously discussed energy shift from (6) will still vanish. Let ψ^0 be any wavefunction definit in parity, then it follows:

$$\begin{aligned}\Delta\mathcal{E} &= 4d_e\langle\psi^0_{_L}|\boldsymbol{S}\cdot\boldsymbol{E}|\psi^0_{_L}\rangle = 4d_e\langle\psi^0_{_L}|P^\dagger P\boldsymbol{S}P^\dagger\cdot P\boldsymbol{E}P^\dagger P|\psi^0_{_L}\rangle \\ &= 4d_e(\pm\langle\psi^0_{_L}|)(+\boldsymbol{S})\cdot(-\boldsymbol{E})\,(\pm|\psi^0_{_L}\rangle) = -4d_e\langle\psi^0_{_L}|\boldsymbol{S}\cdot\boldsymbol{E}|\psi^0_{_L}\rangle = -\Delta\mathcal{E} \\ &\Rightarrow \Delta\mathcal{E} = 0\end{aligned} \tag{7}$$

So it becomes clear that for creating an EDM-induced energy shift, it is necessary to mix states with different parity. Also, the size of the measurable energy shift scales directly with the amount of this mixing.

2.3.6 Atoms in an external electric Field

The eigenfunctions of the Coulomb Hammiltonian (5) without external field ($|\psi^0_{_L}\rangle = |s\rangle,\ |p\rangle,\ \ldots$) are definite in parity. To induce a mixing, it is necessary to apply an external electric field[12]. If the external electric field E_{ext} will be produced in the lab (E_{ext}=E_{lab}), it will be sufficiently weak to enable a perturbatively description of the state mixing. In case of alkali atoms, the wave functions of this system will be given by:[13] [17] [14]

$$\begin{aligned}&|\psi\rangle = \varepsilon_s|s\rangle + \varepsilon_p|p\rangle + \text{ much smaller contributions from higher orbitals} \\ &\text{with } \varepsilon_s \approx 1 \text{ and } \varepsilon_p \approx \frac{\langle s\,|ez|\,p\rangle}{\mathcal{E}(s)-\mathcal{E}(p)}E_{\text{lab}}\end{aligned} \tag{8}$$

This leads to an energy shift proportional to the applied field:

$$\Delta\mathcal{E} = 4d_e\langle\psi_{_L}|\boldsymbol{S}\cdot\boldsymbol{E}|\psi_{_L}\rangle = d_e\left(8\frac{\langle s_{_L}|\boldsymbol{S}\cdot\boldsymbol{E}|p_{_L}\rangle\ \langle s\,|ez|\,p\rangle}{E(s)-E(p)}\right)E_{\text{lab}} \equiv d_eWE_{\text{lab}} \tag{9}$$

W is in most atoms used for eEDM experiments $\gg 1$ and therefore called *enhancement factor*. It can either be understood as the factor relating the electrons eEDM d_e to the atoms aEDM $d_a = Wd_e$, or it can be seen as an enhancement of the applied electric field inside the atom: $E_{\text{eff}} = WE_{\text{lab}}$

Calculations for atomic Cs and Rb yield enhancement factors of $W_{_{Cs}} \approx 120$ and $W_{_{Rb}} \approx 25$ [1]. Laboratory fields are technologically limited to tens of kV/cm. Assuming a value of $d_e = 10^{-30}\,e$cm, one can therefore expect to see an eEDM induced line-shift in Cs of only $\nu \approx 10^{-9}$ Hz.

While early eEDM experiments often used atoms in external electric fields [19][20], modern ones usually try to achieve higher enhancements by utilizing fields inside of molecules [5][21] or crystals [22][23], which can be orders of magnitude higher than the strongest possible lab-fields. This however also means that a perturbative description as

[12] An external magnetic field is not able to mix states with different parity.

[13] Without loss of generality: $\boldsymbol{E}_{\text{lab}}||z$

[14] For example, putting in numbers for Cs ($\langle s\,|ez|\,p\rangle =$ and $\mathcal{E}(s)-\mathcal{E}(p) =$ [18]) and a laboratory field of E_{lab} =10 km, yields $\varepsilon_p \approx 10^{-4}$.

in (8) will not be possible anymore. This makes the calculations for ε_s and ε_p more elaborate and linear proportionality with an external field is not necessarily given anymore. In this case, one is left with the quite general equation:

$$\Delta\mathcal{E} = d_e\, 4\varepsilon_s\varepsilon_p \langle s_{_L}|\boldsymbol{S}\cdot\boldsymbol{E}|p_{_L}\rangle \equiv d_e E_{\text{eff}} \tag{10}$$

The system under investigation in this experiment may possess strong crystal fields, that could mix states of different parity. This mainly depends on the symmetry of the trapping sites inside the Ar matrix (see sec. 4).

2.4 Other CP violating sources in atoms

The previous section started with the general equation for electrons in an electromagnetic potential (1). This is however a simplification in which the effects of the atomic nucleus were approximated with an effective electromagnetic field.

2.4.1 The electron-nucleon coupling C_S

In a more precise theory, the interactions between the nucleus and electrons have to be accounted for directly. One can find three different couplings that are P and CP violating (like the EDM) [9]; namely:

$i(G_F/\sqrt{2})\, C_S \cdot \bar{\phi}\phi\, \bar{\psi}\gamma^5\psi$	scalar-pseudoscalar
$i(G_F/\sqrt{2})\, C_T \cdot \bar{\phi}\sigma^{\mu\nu}\phi\, \bar{\psi}\sigma^{\mu\nu}\gamma^5\psi$	tensor-pseudotensor
$i(G_F/\sqrt{2})\, C_P \cdot \bar{\phi}\gamma^5\phi\, \bar{\psi}\psi$	pseudoscalar-scalar

Here ϕ is the nucleon and ψ the electron field. C_S, C_T and C_P are the different coupling constants for these interactions and $G_F = 1.17{\times}10^{-5}\,\text{GeV}^{-2}$ [24] is the Fermi constant. Of these three, C_S is the most dominant one in paramagnetic atoms like the ones considered for this experiment [9]. Its electron one particle Hamiltonian is given by [6]:

$$H_{C_S} = \frac{iG_F}{\sqrt{2}} A C_S \gamma^0\gamma^5\delta(\boldsymbol{r}) \tag{11}$$

Here A is the nucleon number and $\delta(\boldsymbol{r})$ is the Dirac Delta function. Analogous to d_e, the expectation value of H_{C_S} will vanish for states of definite parity due to the odd parity of $\gamma^0\gamma^5$. If the eigenstates of the undisturbed atom again get mixed by an external electric field into $|\psi\rangle = \varepsilon_s|s\rangle + \varepsilon_p|p\rangle$, the scalar-pseudoscalar nucleon-electron coupling induces an energy shift of:

$$\Delta\mathcal{E}_{C_S} = C_S\left(\varepsilon_s\varepsilon_p \frac{iG_F}{\sqrt{2}} A\langle s|\gamma^0\gamma^5\delta(\boldsymbol{r})|p\rangle\right) \equiv C_S\,\tilde{E}_{\text{eff}} \tag{12}$$

2.4.2 Total CP-violating energy shift

(12) together with (10) leads to the total Energy shift for the dominant sources of CP violation in paramagnetic atoms:

$$\Delta\mathcal{E}_{\not{CP}} = (d_e \cdot E_{\text{eff}} + C_S \cdot \tilde{E}_{\text{eff}}) \tag{13}$$

As previously, the external electric field E_{lab} can be factored out if it is weak enough to allow for a perturbative treatment:

$$\Delta\mathcal{E}_{\not{CP}} = (d_e\, W + C_S\, \widetilde{W}) E_{\text{lab}} \equiv d_{\text{eff}} E_{\text{lab}} \tag{14}$$

C_S, therefore, plays a very similar role to d_e and a possible found CP violating energy shift in one system would not provide information on which of the two caused it.
New very recent calculation for the value of C_S inside of the SM yields $C_S = 6.9{\times}10^{-16}$ [25]. Calculations for $\widetilde{W}$ in the ground state of a free Cesium atom on the other hand yield $\widetilde{W} = 7.59{\times}10^{-19}\, e\,\text{cm}$ [26]. Combining these values for the present thesis yields an effective EDM of:

$$\text{Cesium: } d_{\text{eff}}^{\text{SM}} \simeq 5.2{\times}10^{-34}\, e\,\text{cm} \tag{15}$$

This dwarfs the prediction of d_e in the SM of $d_e \sim 10^{-39}\, e\,\text{cm}$ [2].
Having these multiple contributions is in principle not a problem. Finding a value for (14) that is above (15) would hint at new physics independent of where the CP violation origins from. At some point, it might however be necessary to identify the individual contributions of d_e and C_S to determine which of the numerous new physics models is correct. Then it will definitely be of advantage to have a number of different experiments with different atomic and molecular species for which E_{eff} and $\tilde{E}_{\text{eff}}$ will differ.

2.4.3 Sensitivities to more CP violating parameters

Even the nucleon-electron interaction discussed at the beginning of this section is a simplification. In an even more general theory, the constituting quarks of the nucleons and their interaction with each other and with the electrons have to be taken into account. The up, down, and strange quarks that are the dominant flavors in nucleons can themselves have electric dipole moments (d_u, d_d, d_s). As carriers of colour-charge they can also additionally have color dipole moments ($\tilde{d}_u, \tilde{d}_d, \tilde{d}_s$). Another important source of CP-violation in the strong sector is the vacuum angle of the strong force $\bar{\theta}$ (see sec. 8).
performing an EDM measurement on an atomic or molecular system will in general put constraints onto a multi-dimensional space of CP-violating parameters [6]. Diamagnetic atoms (like Hg, Xe, ...) are more sensible to nuclear CP violating sources and the tensor-pseudotensor electron-nucleon coupling C_T, while Paramagnetic ones (like Cs, ThO, HfF+, ...) put stronger constraints on d_e and the scalar-pseudoscalar electron-nucleon interaction C_S. It is therefore helpful to perform EDM measurements on a lot of different species to reduce the volume of this space as much as possible. One of today's measurements with the highest impact on this space is the spectroscopy on Hg performed by the Heckel group [27] together with the eEDM measurement in ThO by the ACME II experiment[5].

2.4.4 Sensitivities to *even more* CP violating parameters

Apart from these sources of CP violation in the constituents of matter (electrons, protons, neutrons, atoms), EDMs of the other SM particles (muon, tauon, heavy quarks, mesons, and baryons) are of interest too. Their greater masses make them more sensitive to new heavy particles beyond the SM. Also, models that expect more differences between generations like the violation of lepton universality require tests of the EDMs of all the known particles. But even for some of these particles that naively are not contained in conventional matter, atomic and molecular experiments can provide very strong bounds. That is because the heavier SM particles are always present in virtual form, which enables a certain level of sensitivity to possible EDMs of these. In [28], [29] it was shown that the electron EDM measurement with the highest sensitivity to this day, performed in ThO at ACME II, provides limits to the EDMs of the two heavier leptons of

$|d_\mu| < 1.7{\times}10^{-20}\,e\,\text{cm}$ and $|d_\tau| < 1.1{\times}10^{-18}\,e\,\text{cm}$. This already surpasses the sensitivity of the current best high energy searches with the μEDM limit ($|d_\mu| < 1.8{\times}10^{-19}\,e\,\text{cm}$) set at the Brookhaven g-2 experiment [30] and the τEDM ($\text{Re}(d_\tau)$=$(-0.62{\pm}0.63){\times}10^{-17}\,e\,\text{cm}$ and $\text{Im}(d_\tau)$=$(-0.40{\pm}0.32){\times}10^{-17}\,e\,\text{cm}$) reported by the Belle collaboration [31].

Additionally, in [32], [29], limits for the charm and bottom quark electromagnetic and color EDMs from the ACME II results are reported. In [33][34], the current eEDM limits are used complementary to LHC measurements to investigate the complex coupling constants between the 125 GeV Higgs Boson and Fermions. Besides searches for all these new forms of CP-violation, eEDM results can also be used to put new bounds on sources of CPT-violation [35].

2.5 EDM theory conclusions

In this section, it was demonstrated how an eEDM can arise from breaking of CP-symmetry. Further, it was shown how even though the energy shift introduced by d_e in atoms vanishes in the non-relativistic limit, it will nonetheless be possible to measure it when relativistic effects are taken into account. It was also shown, that it is additionally necessary to mix atomic states with different parity to obtain a non-zero energy shift. The amount of this mixing together with the nuclear charge of the used atoms are the main parameter that govern the size of this energy shift.
Following this, it was explained how different levels of complication of the underlying theory lead to more and more sources of CP-violation that could manifest in an atom and cause atomic EDMs orders of magnitude above what is predicted in the SM. This abundance of sensitivities makes it clear why EDM searches belong to the most power full tools in searches for new physics in modern days. Most theories that extend the SM to answer the open questions in the fundaments of physics, require new sources of CP-violation [36] and in turn, most of these would be detectable in EDM measurements.

3 Measuring the eEDM

In the following, a short discussion on how to measure the eEDM will be presented. The goal is to understand which system parameters need to be maximized to reduce statistical uncertainties.
Afterward, an overview of previous solid-state eEDM measurements will be presented to understand how to perform a future measurement and which systematics needs to be avoided.

3.1 Spectroscopy-measurement

The Energy shifts of atomic states, that arise in an environment of electric and magnetic fields, are given by:

$$\Delta\mathcal{E} = \mu\boldsymbol{B}\cdot\boldsymbol{\sigma} + d_e\boldsymbol{E}_{\text{eff}}\cdot\boldsymbol{\sigma} \tag{16}$$

with the magnetic moment μ, the Pauli matrices $\boldsymbol{\sigma}$, and the effective electric field as defined in sec. 2.3.6 $\boldsymbol{E}_{\text{eff}}$. The form of this equation ensures that μ and d_e will always be parallel.

In a spectroscopy measurement, one can now attempt to determine this energy shift by measuring the transition between two states with opposite spin orientations (spin$||\sigma$). The change of the transition energy under $\boldsymbol{E}_{\text{eff}} \rightarrow \boldsymbol{E}_{\text{eff}}$ will be equal to $2\, E_{\text{eff}}\, d_e$.
The magnetic field $\boldsymbol{B}$ can be used to modify the transition energy through the Zeeman effect. It is however important to have very precise control of it. Because $d_e/\mu \ll 1$ [15], already small changes in the magnetic field, will produce backgrounds order of magnitude above the actual eEDM signal.

While in previous solid-state systems, this spectroscopy was done with electric paramagnetic resonance (see sec. 3.4.1), most modern in-beam measurements, like ACME II, use Ramsey spectroscopy instead.

3.2 Magnetometry

Apart from this spectroscopic scheme, there exists also another measurement approach to detect a non-zero eEDM. It makes use of the fact that d_e and μ have to lie on the same axis (see sec. 2.3.2). This has the consequence of coupling electric and magnetic fields $\boldsymbol{E}$ and $\boldsymbol{B}$ that surround the atom in the following way:

Applying a strong $\boldsymbol{E}$ or $\boldsymbol{B}$ field to a sample containing unpaired electrons will align their eEDMs **and** spins into the direction of this field. The organized spins lead to a macroscopic $\boldsymbol{B}$ and the organized eEDMs to a macroscopic $\boldsymbol{E}$ field. This means an applied $\boldsymbol{B}$ field induces a detectable $\boldsymbol{E}$-field and reverse. The sensitivity of this kind of measurement scales linearly with the magnetic susceptibility $\bar{\chi}$.
The amount of polarization P created by the applied field will depend on the population ratio of the two states with different σ. It is generally given by the Boltzmann distribution:

$$P \propto e^{-\frac{\Delta\mathcal{E}}{k_B T}} \tag{17}$$

with the Boltzmann constant k_B and the temperature T. It becomes therefore clear that the electric field magnetization needs to be measured at very low temperatures due to the minuscule value of $\Delta\mathcal{E}$. For the reverse case where a voltage from an applied magnetic field is measured, this is less critical due to the generally much larger energy splitting arising from μB.

3.3 Statistical uncertainty of an eEDM measurement

Generally, the statistical uncertainty of a single measurement is given through the Heisenberg time-energy uncertainty:

$$\Delta\mathcal{E} \cdot \Delta t \sim \hbar \;\Leftrightarrow\; E_{\text{eff}} \Delta d_e \cdot \sqrt{\tau t} \sim \hbar$$
$$\Rightarrow \Delta d_e \sim \frac{\hbar}{E_{\text{eff}} \sqrt{\tau t}}$$

[15] in natural units with c=1

where τ is the decoherence time of the species and t is the total time of measurement. For measurements on N independent atoms, it follows from Gaussian error propagation:

$$\Delta d_e \approx \frac{\hbar}{E_{\text{eff}}\sqrt{\tau t\, N}} \tag{18}$$

This equation can be used for spectroscopy and magnetometry measurements alike[37]. It becomes clear, that it is desirable to increase all these parameters as far as possible to get the lowest possible statistical uncertainty.
As discussed previously in sec. 2.3.6, the size of E_{eff} can be increased by mixing states of different parity as much as possible and by picking a species with high nuclear charge Z. One parameter that can vary by many orders of magnitude between experiments is N. The number of accessible atoms/molecules in a solid state system is much higher than what is achievable in a beam of atoms/molecules. Even between solid-state samples, N can dramatically vary depending if the probed atoms are an integral part of the crystal structure or just dopants in a larger matrix.
Another advantage of cryogenic matrices lies in the high decoherence times that are achievable in them. The Weinstein group for example measured a decoherence time of $\tau = 0.1s$ on Rb doped para-hydrogen[38]. This is two orders of magnitude higher than τ in the currently most successful measurement, ACME II[5].

Altogether, eEDM measurements in cryogenic matrices open the possibility to push the sensitivity to d_e orders of magnitude beyond the current best values. This however requires first to create samples with all these advantageous properties. Afterward, there will as well be the challenge of suppressing systematic errors to the level of the statistical errors.

3.4 History of eEDM measurements in solid state system

In this section, an overview of the eEDM measurements in solids that have been performed so far is provided. Because the sensitivity of solid-state measurements has been always behind the most successful methods of their time, they are often, if at all, only mentioned as a side note.
For the topic of this thesis, it is however of interest to understand the challenges that these experiments faced to plan future measurements in our solid-state setup accordingly. A summary[16] of the results that have been achieved in solid state systems over the years, can be found in table 2.

3.4.1 EPR measurements in the 1960s

The first successful eEDM search in a solid system was performed 1961 by M. E. Browne on mono-crystalline $KCr(SO_4)_2\ 12H_2O$ and $NH_4(SO_4)_2\ 12H_2O$ at cryogenic temperatures [39].
The measurement was performed with a modified version of electron paramagnetic resonance (EPR). While in regular EPR, one exposes a sample to microwave radiation and ap-

[16]To my knowledge this is the first time that all these measurement results are compiled together. Especially the two measurements from the 1960s seem to be mostly forgotten in the EDM community and are for example not mentioned in the reviews [6] and [7].

year	sample	eEDM limit in e·cm	method	
1961	KCr- & NH_4- $(SO_4)_2$ $12H_2O$	$d_e < 10^{-13}$	EPR spectroscopy	[39]
1963	Al_2O_3:Cr & MgO:Cr	$d_e = (1\pm4.6)\times10^{-16}$	EPR spectroscopy	[40]
1979	nickel-zink-ferrite	$d_e = (8.1\pm11.6)\times10^{-23}$	Magnetometry	[41]
2004	GdIG	$d_e = (2\pm3)\times10^{-24}$	Voltage measurement	[42]
2011	GGG	$d_e = (-5.57\pm7.98_{\text{stat}}\pm0.12_{\text{syst}})\times10^{-25}$	Magnetometry	[43]
2012	$Eu_{0.5}Ba_{0.5}TiO_3$	$d_e = (-1.07\pm3.06_{\text{stat}}\pm1.74_{\text{syst}})\times10^{-25}$	Magnetometry	[44]

Table 2: eEDM searches in solid state systems that published results on d_e-bounds

plies a magnetic field to measure the energy splitting due to the Zeeman effect[17], Browne instead applied an electric field to measure the linear stark splitting due to the eEDM (see eq. 16). From measuring no E-field induced line-broadening (let alone line splitting), he was able to provide an upper bound on the value of d_e.

Two years later, in 1963, E. B. Royce and N. Bloembergen improved on this measurement by using Al_2O_3:Cr and MgO:Cr [40]. These have much higher enhancement factors, due to more asymmetric trapping sites. Instead of just an electric, the authors applied parallel electric and magnetic fields together. The magnetic field now already splits up the degeneracy of the resonance. Therefore the effect of $d_e E_{\text{eff}}$ can now be measured as a line shift instead of just a line-broadening.
As the most significant uncertainties in their measurement, Roye, and Bloembergen named the instability of the applied fields and the unavailability of reliable theoretical techniques to calculate the crystal fields in their samples.

At their time, the precision of these measurements was only one order of magnitude below the leading ones. Nonetheless, after these two works, no other works on eEDM searches with EPR in solids have been published. It seems like the interest in the field focused more on measurements of the magnetoelectric effect (see. sec. 4).

3.4.2 Magnetometry measurements

The idea to measure the eEDM with the method of magnetometry (see sec. 3.2) was first suggested by F. L. Shapiro in 1968 [45]. The first measurement was performed on a ferromagnetic sample of nickel-zink ferrite (NZF) by B. V. Vasil'ev and E. V. Kolycheva in 1978 [41]. They applied an oscillating electric field onto the NZF and used a SQUID[18] to measure the magnetization arising from the eEDM-induced sample polarization. The authors also attempted a measurement on EuO. It however has not been able to sustain the applied electric field.
Vasil'ev and Kolycheva named large sources of noise and drifts in all their electronics as

[17]For most EPR measurements a static magnetic field is superimposed with a small oscillating field. This enables lock-in amplification leading to increased precision. The resulting signal is the first derivative of the initial absorption peak.

[18]superconducting quantum interference device

the most significant sources of errors. They also reported difficulties in maximizing the magnetic-field-pickup for the SQUID

Only more than 20 years later, the method of measuring the magnetic field induced by the polarization of eEDMs, got picked up again by S. K. Lamoreaux [22]. He kicked off two new magnetometry measurements.
The first was performed on paramagnetic Gadolinium-Gallium-Garnet (GGG) at $4\,\mathrm{K}$. It featured an improved pick-up-coil design with two orders of magnitude higher sensitivity compared to Vasil'ev and Kolycheva. Additionally, two identical samples were probed at the same time to further reduce systematics. The authors report that they were able to suppress all sources of noise, below the one of the SQUID. They proposed to repeat the measurement with a larger sample at sub-Kelvin temperatures and a lower noise SQUID. According to their projections, this would push the sensitivity of a future measurement to the same level as in-beam experiments. It seems this was however never attempted afterward.

Another measurement carried out at almost the same time, used $Eu_{0.5}Ba_{0.5}TiO_3$ [44]. In comparison to GGG, this material has less symmetry which allows for ferroelectric order, namely ferroelectricity[19]. Due to this ferroelectricity, there is a much higher internal electric field inside the sample, leading to a $\sim$ 700 times higher enhancement factor. This however also leads to larger magnetoelectric couplings (see sec. 4). They created the largest source of systematics for this experiment. Another problem appeared in form of the ferroelectric relaxation. After being exposed to an electric field, the ferroelectric needs some time to get fully polarized. During this time, small currents flow in the sample, which in term produce magnetic fields much larger than the expected eEDM response.
Despite these difficulties, the measurement in $Eu_{0.5}Ba_{0.5}TiO_3$ was still able to increase the limit measured in GGG slightly (see table 2).
To this day, this provides the most stringent limit on d_e set in a solid state experiment. A predecessor to these solid state magnetometry experiments, is CASPEr electric [46]. CASPEr is not sensitive to constant eEDMs but instead to time-varying ones, which makes it sensitive to axions (see sec. 8).

3.4.3 Measurement of electric fields induced by the eEDM

There has been only one attempt to measure the eEDM-induced electric potential after application of a magnetic field. It as well has been proposed by S. K. Lamoreaux and performed at Amherst College, Massachusetts.
In the experiment, ferrimagnetic gadolinium-iron-garnet (GdIG) was used. Two samples of this material were doped with different amounts of Yttrium to achieve specific compensation temperatures[20]. That way, they were able to create a combined system in which the effect of the eEDM always canceled except for the range between the two compensation temperatures. This enables to compare situations with and without eEDM-effect to

[19] A ferroelectric possesses a permanent electric field (similar to a ferromagnet, which has a permanent magnetic field)

[20] The compensation temperature of a Ferrimagnet, is the temperature where the magnetization of its sub-lattices exactly cancel out.

subtract backgrounds. The current created by the small potential difference arising from polarized eEDMs was picked up with a JFET[21].
The largest complication in this measurement was the pinning of magnetic domains which did not align to the external magnetic field. This effect was much stronger than the authors expected beforehand, drastically limiting the sensitivity of their measurement.

3.4.4 eEDM measurements in cryogenic matrices

The idea of using atoms implanted in cryogenic matrices to measure the eEDM was first proposed by C. Pryor and F. Wilczek in 1987 [47].

The first experimental investigations were undertaken by the group around A. Weis in the time between 1990 and 2010 [48][49][50]. They implanted Cs and Rb atoms in solid ^{4}He [22]. Afterward, the Group around J. D. Weinstein started to pursue a number of measurements on Rb embedded in Ar, Ne, and para-hydrogen, that are still ongoing today. These are however not aimed on measuring d_e.

Over the last few years, new groups began preparing eEDM measurements in cryogenic matrices. The first is called EDM^3 and is based in Toronto. In their project, BaF molecules will be implanted in solid Ar and Ne[23][51]. This has the potential advantage of profiting from huge intra-molecular field enhancements analogous to modern-day in-beam experiments. a second is based in Padua and uses Rb in Ar & Ne [52], as well as BaF in para-hydrogen [53]. a third was formed by G. Gabrielse. They want to investigate WC (tungstene-carbide) molecules dispersed in solid parahydrogen[54]. Finally, there is the EDMMA collaboration based in Paris, that runs the experiment presented in this thesis.

3.4.5 Conclusions from previous solid-state measurements

For eEDM measurements of alkali atoms embedded in noble-gas matrices, optical measurements, like they were performed in the 1960s, seem most reasonable. Even though magnetometry measurements yielded the most precise results to this day, it is unlikely that the low densities of alkali atoms in matrices can compete with bulk crystals. The same goes for magnetic-field induced voltage measurements.
The possibility to perform further magnetometry studies on bulk crystals, as was suggested for GGG, seems however still intriguing.
The same goes for new voltage measurements. Because the main issue in the GdIG measurement has been the switching of magnetic fields, it could be interesting to achieve the high polarization in another way. For example with optical pumping techniques.

Looking at all these past measurements, it becomes clear how important the effects of magnetoelectric order are. For that reason, this topic will be discussed in more detail in the next section.

[21] junction field effect transistor

[22] Creating samples out of ^{4}He is quite different from growing matrices out of the other noble gases. This is because ^{4}He will not undergo the phase transition to a solid unless a high pressure is applied. Depositing ^{4}He together with dopants on a window like it was done for this thesis, is, therefore, not possible.

4 Electromagnetic field mixings in solids

Because the energy shift in the atoms depends both on the coupling of the eEDM to the $\boldsymbol{E}$-field and on the coupling of the magnetic moment μ to the $\boldsymbol{B}$-field, it is important to also consider possible mixings between both fields. These so-called magnetoelectric mixings can have a number of microscopic origins [55]. For example, an displacement of atoms induced by an external electric field can deform electron orbitals in a way that the spin-orbit coupling becomes anisotrope. This slightly polarises them, causing a magnetic field [56].

magnetoelectric mixings break spacial symmetries and are for this reason, only allowed in environments with the same symmetry-breaking behavior. Therefore, knowing the crystal group of the crystal around the implanted atoms (trapping site symmetry), gives information on the $\boldsymbol{E}$-$\boldsymbol{B}$ mixing tensors.

The general internal electric and magnetic fields $\boldsymbol{E}^{\text{int}}$ and $\boldsymbol{B}^{\text{int}}$ that are created by the mixings of applied external fields $\boldsymbol{E}^*$ and $\boldsymbol{B}^*$ are given by:[23] [24]

$$E_i^{\text{int}} = E_i^* + \tfrac{1}{\varepsilon_0} P_i^{\text{stat}} + \chi_{ij} E_j^* + \alpha_{ij} B_j^* + \tfrac{1}{2}\beta_{ijk} B_j^* B_k^* + \gamma_{jki} B_j^* E_k^* + \chi^{(2)}_{ijk} E_j^* E_k^* \quad (19)$$

$$B_i^{\text{int}} = B_i^* + \mu_0 M_i^{\text{stat}} + \bar{\chi}_{ij} B_j^* + \alpha_{ji} E_j^* + \beta_{ijk} E_j^* B_k^* + \tfrac{1}{2}\gamma_{jki} E_j^* E_k^* + \bar{\chi}^{(2)}_{ijk} B_j^* B_k^* \quad (20)$$

$\boldsymbol{\alpha}$, $\boldsymbol{\beta}$ and $\boldsymbol{\gamma}$ are tensors mixing $\boldsymbol{E}^*$ and $\boldsymbol{B}^*$. $\boldsymbol{\chi}$, $\boldsymbol{\chi}^{(2)}$, $\bar{\boldsymbol{\chi}}$ and $\bar{\boldsymbol{\chi}}^{(2)}$ are the linear and 2nd-order electric and magnetic susceptibility tensors[25].

As previously discussed in sec. 3, the energy shift in an eEDM experiment, is generally given by:

$$\Delta\mathcal{E} = \sigma_i (d_e E_i^{\text{int}} + \mu B_i^{\text{int}}) \quad (21)$$

4.1 The magnetoelectric mixing $\boldsymbol{\alpha}$

Looking at the different mixing tensors, it becomes clear that mixing tensor $\boldsymbol{\alpha}$ is probably the most dangerous in an eEDM experiment as it can lead to a signal proportional to μ, indistinguishable from d_e:

$$\Delta\mathcal{E} = \sigma_i (d_e E_i^* + \mu\alpha_{ij} E_j^* + ...) \quad (22)$$

Because the eEDM is so small, it is likely that $\mu\alpha_{ij}$ (if allowed by the crystal symmetry) could be orders of magnitude larger than d_e.

[23] It would be more correct to use the electric displacement field $\boldsymbol{D}$ and the magnetizing field $\boldsymbol{H}$. For better analogy to atomic physics systems, I, however define $\boldsymbol{E}^{\text{int}} = \boldsymbol{D}/\varepsilon_0$ and $\boldsymbol{B}^* = \mu_0 \boldsymbol{H}$. ε_0 is the vacuum permittivity and μ_0 the Vacuum permeability. Further, I use $c = \frac{1}{\sqrt{\varepsilon_0 \mu_0}} = 1$.

[24] only terms up to order 3 are considered here. Higher order terms are very rare and will therefore be neglected in the following.

[25] As pointed out in [55] and [57], this expression also already implicitly includes the effects of toroidal mixings.

For that reason, previous experiments searching for the eEDM in solids with the method of magnetometry [41][58][59][60] put large emphasis on choosing a symmetric sample without magnetoelectric order. This can potentially be a disadvantage as this limits the choice to relatively symmetric samples that in turn possess less parity violating mixings. However, because α_{ij} is a tensor coupling, the created false signal is in many cases actually not parallel to $d_e\,\sigma_i$. Only non-zero diagonal entries α_{ii} have this effect. This opens up some possibilities to distinguish both.

4.2 Quadratic mixings

In the following, I will derive a way how one can eliminate all even order effects (quadratic couplings and static magnetization/polarization) by measuring the energy shift from four different field orientations:

Following from (21), the energy shift in a crystal under the influence of fields $\boldsymbol{E}^*$ and $\boldsymbol{B}^*$, is given by:

$$\begin{aligned}\mathcal{E}(\boldsymbol{E}^*,\boldsymbol{B}^*) = \sigma_i \cdot [d_e\,(E_i^* + \tfrac{1}{\varepsilon_0}P_i^{\text{stat}} + \chi_{ij}E_j^* + \alpha_{ij}B_j^* + \tfrac{1}{2}\beta_{ijk}B_j^*B_k^* + \gamma_{jki}B_j^*E_k^* + \chi^{(2)}_{ijk}E_j^*E_k^*)\\ + \mu(B_i^* + \mu_0 M_i^{\text{stat}} + \bar{\chi}_{ij}B_j^* + \alpha_{ji}E_j^* + \beta_{ijk}E_j^*B_k^* + \tfrac{1}{2}\gamma_{jki}E_j^*E_k^* + \bar{\chi}^{(2)}_{ijk}B_j^*B_k^*)]\end{aligned}$$

In a first step, it is possible to eliminate all terms that are not linear in $\boldsymbol{E}^*$, by reversing its direction:

$$\tfrac{1}{2}[\mathcal{E}(\boldsymbol{E}^*,\boldsymbol{B}^*) - \mathcal{E}(-\boldsymbol{E}^*,\boldsymbol{B}^*)] = \sigma_i[d_e(E_i^* + \chi_{ij}E_j^* + \gamma_{ijk}B_j^*E_k^*) + \mu(\alpha_{ij}E_j^* + \beta_{ijk}E_j^*B_k^*)]$$

This however still leaves dependencies on $\boldsymbol{\beta}$ and $\boldsymbol{\gamma}$. Both are invariant under simultaneous inversion of $\boldsymbol{E}^*$ and $\boldsymbol{B}^*$. Therefore:

$$\begin{aligned}&\tfrac{1}{4}([\mathcal{E}(\boldsymbol{E}^*,\boldsymbol{B}^*) - \mathcal{E}(-\boldsymbol{E}^*,\boldsymbol{B}^*)] - [\mathcal{E}(-\boldsymbol{E}^*,-\boldsymbol{B}^*) - \mathcal{E}(\boldsymbol{E}^*,-\boldsymbol{B}^*)])\\ &= \sigma_i[d_e(E_i^* + \chi_{ij}E_j^*) + \mu\alpha_{ij}E_j^*]\end{aligned} \tag{23}$$

This combination of measurements makes it possible to reduce the initial 14 terms from above to only 3.

However, avoiding coupling terms altogether is more favorable than eliminating them this way. Depending on fluctuations and imperfect inversion of $\boldsymbol{E}^*$ and $\boldsymbol{B}^*$, quadratic terms could still produce enough noise and backgrounds to overshadow the signal from d_eE^* completely. As before for $\boldsymbol{\alpha}$, off-diagonal terms in the tensors $\boldsymbol{\beta}$ and $\boldsymbol{\gamma}$ are much more favourable than on-diagonal ones.

For these reasons, it is essential to understand the particular situation in our experimental system of Cs doped Ar, to evaluate how much danger the magnetoelectric effect poses.

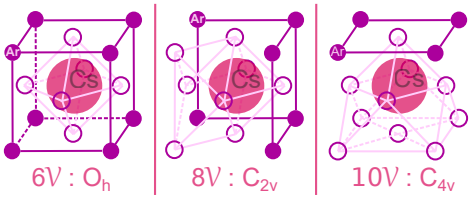

Figure 3: Possible trapping site symmetries of the Cs atoms inside the Ar matrix.

4.3 Possible trapping site symmetries of Cs in Ar

Argon naturally forms an fcc-structure[26] structure. In [61], a simulation on the number of Ar vacancies $\mathcal{V}$ depending on the interaction with the trapped species was performed. Because the atoms in such a system bind through the Van-der-Waals interactions, the interaction potentials V were approximated with the Lennard-Jones potential:

$$V_{LJ}(r) = \epsilon \left[\left(\frac{\rho}{r}\right)^{12} - 2\left(\frac{\rho}{r}\right)^{6} \right] \tag{24}$$

ϵ and ρ are the free parameters describing the shape of the individual binding. ϵ gives an indication of the potential depth, while ρ quantifies the position of its minimum. Combining the potential of Cs atoms [62] with the results from the simulation, yield the following trapping sites as most likely:

$$6\mathcal{V} : O_h \quad | \quad 8\mathcal{V} : C_{2v} \quad | \quad 10\mathcal{V} : C_{4v} \tag{25}$$

with the number of vacancies $\mathcal{V}$ followed by the crystal group. An illustration of the geometry of these trapping sites is shown in fig. 3.

In [56] an overview of the electromagnetic couplings of the different crystal groups is presented. From it, the following tensors $\boldsymbol{\alpha}$ can be extracted:

$$\boldsymbol{\alpha}^{O_h} = \begin{pmatrix} 0 & 0 & 0 \\ 0 & 0 & 0 \\ 0 & 0 & 0 \end{pmatrix}, \quad \boldsymbol{\alpha}^{C_{2v}} = \begin{pmatrix} 0 & \alpha_{12} & 0 \\ \alpha_{12} & 0 & 0 \\ 0 & 0 & 0 \end{pmatrix}, \quad \boldsymbol{\alpha}^{C_{4v}} = \begin{pmatrix} 0 & \alpha_{12} & 0 \\ -\alpha_{12} & 0 & 0 \\ 0 & 0 & 0 \end{pmatrix}$$

From investigations in [63], it follows that for O_h, C_{2v} and C_{4v} all restrictions that exist on the tensor $\boldsymbol{\beta}$, are the same as the ones on $\boldsymbol{\gamma}$. Generally $\boldsymbol{\beta}$ and $\boldsymbol{\gamma}$ are 3rd rank tensors with 27 entries each. In the case of O_h, C_{2v} and C_{4v} the tensors are however quite sparse [56]. Their components λ_{ijk} have to comply with the following restrictions:

$$\begin{aligned} O_h &: \ \lambda_{ijk} = 0 \\ C_{2v} &: \ \lambda_{123} = \lambda_{132}, \ \lambda_{213} = \lambda_{231}, \ \lambda_{312} = \lambda_{321}, \ \text{remaining } \lambda_{ijk} = 0 \\ C_{4v} &: \ \lambda_{123} = \lambda_{132} = -\lambda_{213} = -\lambda_{231}, \ \text{remaining } \lambda_{ijk} = 0 \end{aligned} \tag{26}$$

[26] fcc= face centered cubic

4.3.1 Possible field mixings in a Cs doped Ar matrix

From the previous section, it becomes clear that the O_h symmetry does not allow for magnetoelectric field mixings. This makes it an optimal environment for avoiding magnetoelectric background effects.
For both C_{2v} and C_{4v}, the linear mixing tensors $\boldsymbol{\alpha}$ are hollow, and therefore possible mixings will only create field components orthogonal to the direction of the applied fields. Therefore it should be possible to distinguish a signal arising from $\mu\alpha_{ij}$ from the actual eEDM one.

For the higher order couplings $\boldsymbol{\beta}$ and $\boldsymbol{\gamma}$, diagonal terms can also be completely avoided in the case of C_{4v} crystal symmetry. I will express the parallel[27] applied electric and magnetic fields as $\boldsymbol{E}^* = E\hat{f}$ and $\boldsymbol{B}^* = B\hat{f}$ with the normalized vector $\hat{f} = (f_1, f_2, f_3)^\intercal$. Then it follows for $\widetilde{\boldsymbol{E}}^{\text{int}}$ and $\widetilde{\boldsymbol{B}}^{\text{int}}$, the components of $\boldsymbol{E}^{\text{int}}$ and $\boldsymbol{B}^{\text{int}}$ that are created by the $\boldsymbol{\beta}$ and $\boldsymbol{\gamma}$ couplings of $\boldsymbol{E}^*$ and $\boldsymbol{B}^*$:

$$\widetilde{\boldsymbol{E}}^{\text{int}} = \tfrac{1}{2}B^2\left(\beta_{123}f_2f_3, -\beta_{123}f_1f_3, 0\right)^\intercal + EB\left(\gamma_{123}f_2f_3, -\gamma_{123}f_1f_3, 0\right)^\intercal$$
$$\widetilde{\boldsymbol{B}}^{\text{int}} = EB\left(\beta_{123}f_2f_3, -\beta_{123}f_1f_3, 0\right)^\intercal + \tfrac{1}{2}E^2\left(\gamma_{123}f_2f_3, -\gamma_{123}f_1f_3, 0\right)^\intercal$$

These components are however orthogonal to the applied electric field $\boldsymbol{E}^*$[28]:

$$\widetilde{\boldsymbol{E}}^{\text{int}} \cdot \boldsymbol{E}^* = \tfrac{1}{2}EB^2\left(\beta_{123}f_1f_2f_3 - \beta_{123}f_1f_2f_3\right) + E^2B\left(\gamma_{123}f_1f_2f_3 - \gamma_{123}f_1f_2f_3\right) = 0$$
$$\widetilde{\boldsymbol{B}}^{\text{int}} \cdot \boldsymbol{E}^* = E^2B\left(\beta_{123}f_1f_2f_3 - \beta_{123}f_1f_2f_3\right) + \tfrac{1}{2}E^3\left(\gamma_{123}f_1f_2f_3 - \gamma_{123}f_1f_2f_3\right) = 0$$

This way, also 2nd order effects will not directly interfere with an eEDM signal.

The same does not work for C_{2v} due to the reduced symmetries of its tensors $\boldsymbol{\beta}$ and $\boldsymbol{\gamma}$. For it, it will only produce necessarily orthogonal components if $f_1f_2f_3$ is zero. This can only be achieved, by aligning the direction of the external field with the internal crystal axes. For a polycrystalline material, this will however be impossible. Therefore, C_{2v} is the least desirable symmetry of these three.

5 Setup

5.1 Cryostat

The cryostat used in this experiment can operate down to 3.3 K. To reach temperatures that low, a cryostat with high-quality thermal shieldings and a potent cryocooler is required. The cryostat for this experiment was manufactured by *Mycryofirm*. It consists of two cooling stages, that are enclosed in copper shields (fig.4 d,e and fig. 6). They enable efficient heat flux and shield off the thermal radiation emitted by the warmer parts of the cryostat's interior and exterior. For longer durability, the copper shields are plated with gold.

[27] From (16), it becomes clear, that parallel fields are the best choice for an eEDM measurement to maximize its sensibility. Besides this, if $\boldsymbol{E}^*$ and $\boldsymbol{B}^*$ are not parallel, interactions with the nuclear anapole moment (see sec. 9) could additionally disturb the measurement.

[28] And therefore in this case also orthogonal to $\boldsymbol{B}^*$

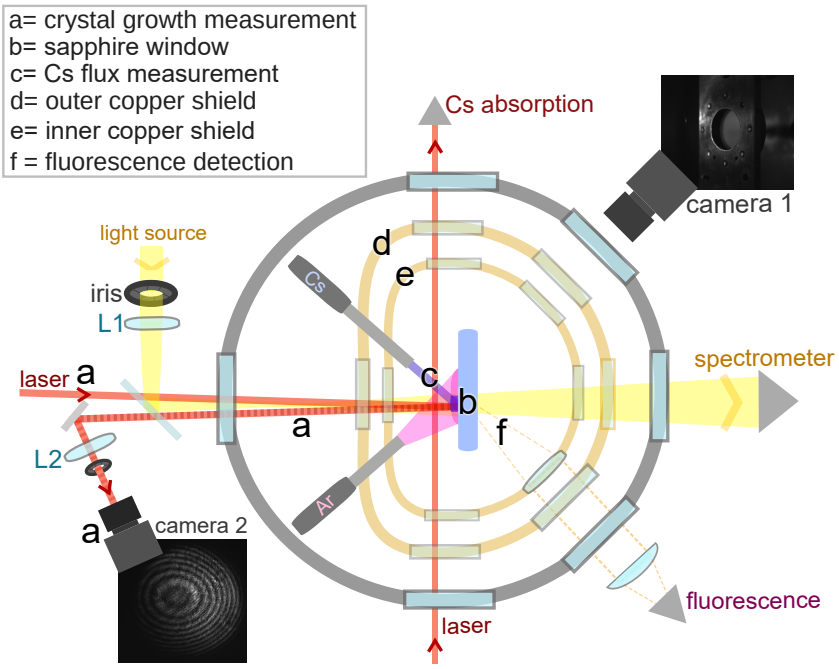

Figure 4: Experimental setup. A Cs doped Ar crystal is formed on the sample holder (**b**) and then probed by different spectroscopic means.

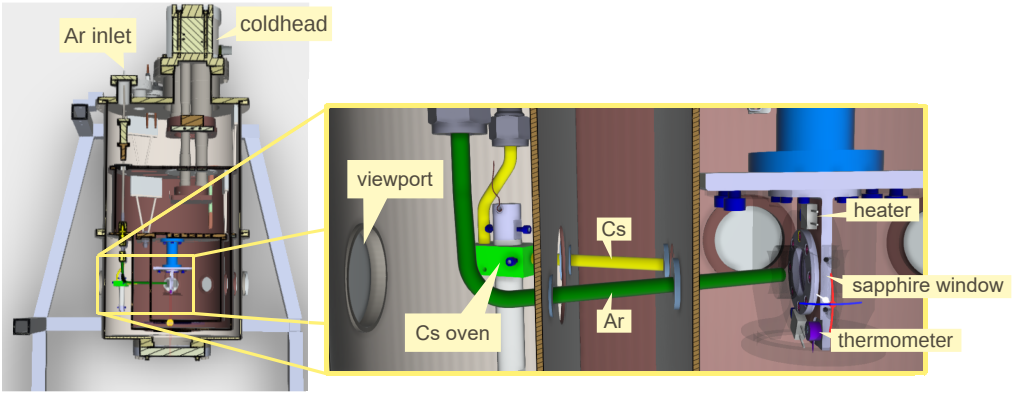

Figure 5: Interior of the cryostat with focus on the matrix deposition.
3D model by Bruno Vivan.

The heat in the setup is pumped out by a *Sumimoto SRP-082B2S Cryocooler*. It uses a closed circuit system of liquid helium that cools down by expansion.
Inside the innermost shield, a sample holder is mounted. It holds a c-cut[29] sapphire window. on it, crystal samples are deposited. To reduce vibrations of the sample holder that could disturb spectroscopic measurements, *Mycryofirm* designed a decoupling system in the upper stage of the setup (fig. 6). It is made from flexible copper cords that efficiently transmit heat, but damp the strong mechanical vibrations of the cold head.

Argon gas is deposited onto the sample holder by a tube that can be connected to a gas bottle on the outside. Its flow is controlled by a mechanical valve.
Atoms of the alkali metals Cs and Rb are deposited from a small dispenser, that is mounted outside of the copper shieldings. Inside it, a small metallic dispenser can be attached. We use commercially available dispensers produced by *AlfaVak* that are filled with ab CsBi40-Alloy (RbBi40). When heated through a current of multiple A pure Cs or Rb gas exits a small slit in these dispensers. From there, the Atoms are guided onto the sample holder by a metallic tube. An overview of the deposition system is shown in fig. 5.
To enable different types of manipulations and monitoring of the sample, six viewports sealed with glass windows are mounted into all three layers of shielding.
For precise temperature control, temperature sensors and resistive heaters are attached to the two cryogenic stages, the sample holder, the argon tube, and the Cs oven. They are monitored and regulated with the *Cryo con 24c temperature controller*. Its PID[30] functionality allows to stabilize the samples temperature with mK precision. Additionally, heating strips are attached to the outside of the setup. These can be used for baking and for keeping the outside above water condensation temperature.

5.2 Laser preparation

The laser for the experiment is produced by an *eagleyard* DFB[31] diode. Its wavelength can be controlled by the diode's temperature and the applied pumping current. This however does not directly provide information on the current wavelengths. Therefore to set the laser to the Cs $6^2S_{1/2} \rightarrow 6^2P_{3/2}$ transition of 852.35 nm[18], an absorption measurement on Cs vapour has to be performed[32]. To increase the resolution of this measurement, the absorption is performed Doppler-free.

In fig. 7, the optical setup for preparation of the laser's wavelength is shown. The pumping current is modified with a function generator to scan through a wide range of frequencies at once.
On the output of the laser, a Faraday-isolator is used to avoid back reflections into the laser. Afterwards, the laser is split up with a polarizing beam splitter (PBS)[33]. the reflected part is used for the wavelength measurement while the transmitted component is

[29] Cut along the c-plane(=[0001]-plane in Bravais-Miller indices). This makes the window non-birefringent along the direction of the incoming light.

[30] **P**roportional, **I**ntegral, **D**erivative

[31] DFB = Distributed FeedBack

[32] This transition is set to measure the Cs flux rate (see sec. 5.4).

[33] The $\lambda/2$ waveplate in front of the PBS is used to control how much of the laser's intensity goes in which direction.

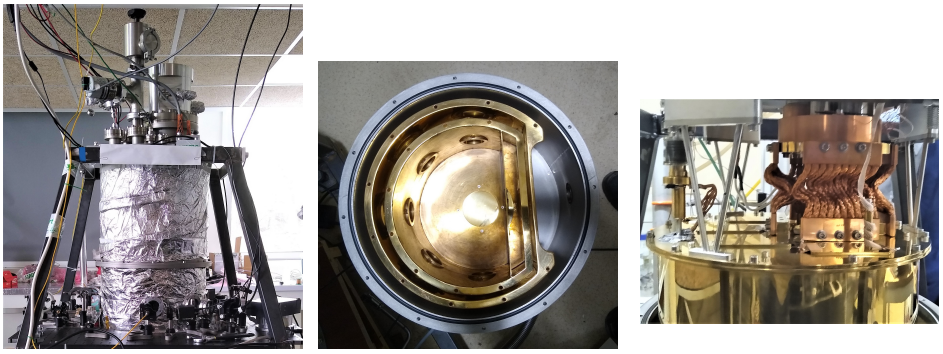

Figure 6: *left:* closed cryostat from the outside. *center:* outer shell of the cryostat together with the two gold plated copper shieldings. *right:* mechanical dampers in the upper stage of the cryostat.

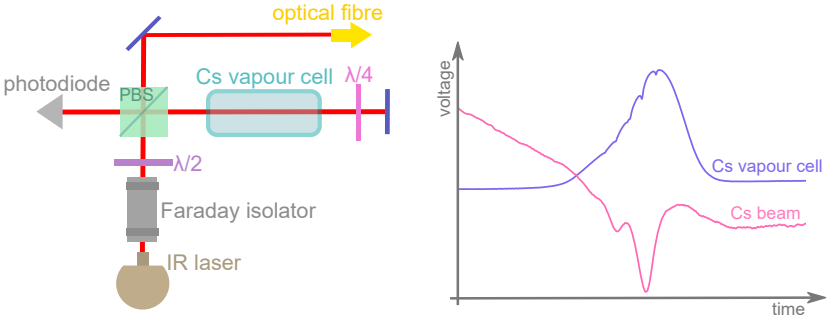

Figure 7: *left:* setup for the laser preparation. *right:* qualitative laser absorptions spectra measured simultaneously in the vapour cell and in the Cs beam (see **c** in fig. 4).

brought through an optical fibre to the cryostat. The reflected component traverses a Cs vapour cell before being reflected back enabling Doppler-free resolution of the hyperfine substructure of the $6^2S_{1/2} \rightarrow 6^2P_{3/2}$-transition[34].

5.3 Measurement of crystal growth rate

To gather information about the crystal thickness, and with it, the dopant density, the growth rate of the Ar crystal has to be measured. Different from previous works [64][65], the change in crystal thickness in this setup, can be measured over a whole 2D section instead of just a single 1D spot.

[34]The $\lambda/4$-plate in front of the mirror acts in total as a $\lambda/2$-plate on the beam. This enables to reach maximal transmission through the PBS later on.

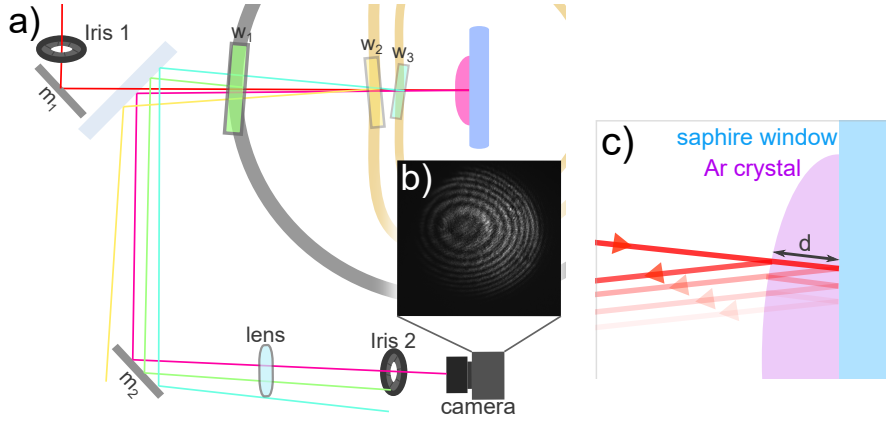

Figure 8: Diagram of the Fizeau crystal thickness detection (**a** in fig.4).
a): setup to separate the interference in the Ar crystal from interferences in other elements of the setup. The laser waist is controlled by iris 1. After interference on the sample crystal, a lens is used to image its surface onto a camera. A second iris can be used to block out light from reflections on viewports W1, W2, and W3.
b): interference pattern of a pure Ar crystal.
c): close-up view of the thin film interference in the Ar crystal.

When a laser with a wide waist hits the semi-transparent Ar-crystal, external and internal reflection occurs similar to a Fizeau interferometer (see fig.8). This process is sometimes referred to as "thin film interference". constructive interference occurs in a situation like this under the condition $2nd(\boldsymbol{x},t)\cos\theta = m\lambda$, with the crystals refractive index n, the local thickness $d(\boldsymbol{x},t)$, the angle of reflection inside the crystal θ, the laser wavelength λ and any natural number m [66]. Because the light enters almost perpendicular, $\cos\theta \approx 1$. During growth, the thickness of the crystal changes with a stable rate $r(\boldsymbol{x})$. This rate can be measured by recording the frequency f in which the interference pattern oscillates at a point $\boldsymbol{x}_0$. It can be easily read off the camera as long as the crystal quality is clean enough. The growths rate $r(\boldsymbol{x})$ is then given by:

$$r(\boldsymbol{x}_0) = \frac{\lambda}{2n} f(\boldsymbol{x}_0) \equiv \kappa f(\boldsymbol{x}_0) \tag{27}$$

The wavelength λ of the DFB laser was set at $0.852\,\mu$m. With the refractive index of Ar: $n_{\mathrm{Ar}} = 1.3$ [67], this gives a constant of $\kappa = 0.33\,\mu$m. For most deposits, the crystal growth rate was around $1\,\mu$m/min at the center of the sample.

Because of the three windows that lead to the sample, there will be a number of unintentional interferometers formed as well. To separate the signal produced by these off from the interference signal of the crystalline sample, the windows were not mounted

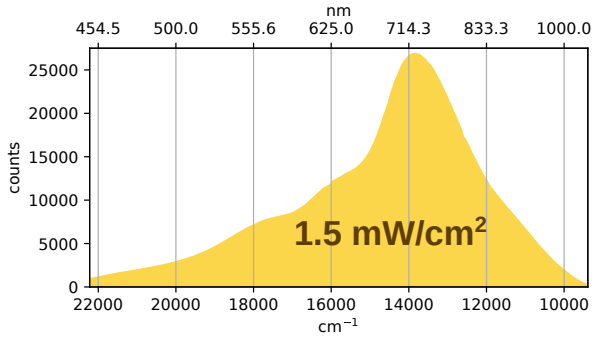

Figure 9: Spectrum of the light source. Its exact shape can differ slightly between measurements depending on the alignment of the light path. The intensity of the light was around 1.5 mW/cm^2.

straight but with a slight angle (see **a** in fig. 8). The correct signal can be isolated, by blocking the others with an iris in front of the camera.

5.4 Alkali flux measurement

Part of the same laser beam that is used to measure the Ar growth rate, is previously split off and used to measure the flux of Cs atoms on their way to the sample. For that, the beam crosses the Cs at an angle of 22°, before being detected in a photodiode. The this way obtained absorption spectrum, can in future studies be used to calculate the density of Cs atoms in the crystalline matrix.
One measured in-beam absorption spectrum can be seen in fig. 7 on the right.

5.5 Transmission Spectroscopy

To study the crystals on the sapphire window, spectroscopy is a very versatile tool. In our setup we use an *Avantes AvaLight-HAL* tungsten-halogen light source together with a *ocean optics qe65000* spectrometer. The light emitted by the lamp is first restricted by an iris which is then imaged onto the sample by a lens (see fig. 4). Its diameter can be controlled by an iris and its position on the sample can be monitored with the two cameras. This gives control to precisely choose the region of the crystal sample to be probed.
Because the spectrum emitted by the lamp is not flat (see fig. 9) in wavelength, for most studies, it is helpful to normalize the taken spectra through an initial one. That way, the change in absorption during different manipulations can be studied.

5.6 Spectrometer calibration

To interpret the measured data, it is necessary to calibrate the spectrometer. For this, the absorption peaks of a Hg and a Xe gas discharge tube, the laser wavelength on the

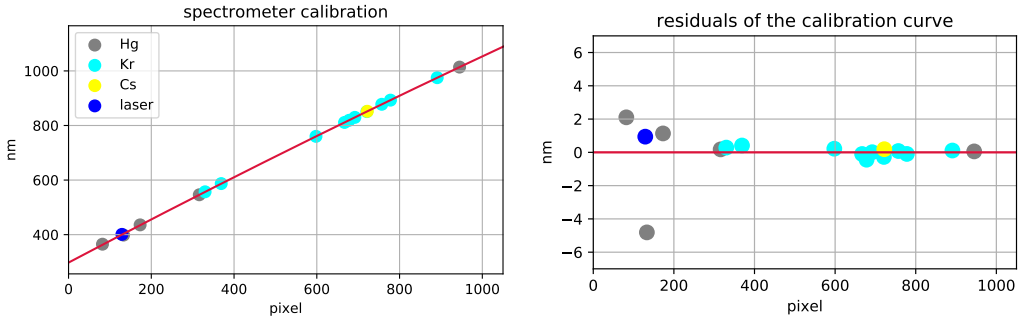

Figure 10: Calibration measurement of the spectrometer. the recorded output in pixel is plotted against literature values for the wavelength. The red curve fits the data points with a 3rd-degree polynomial. On the right, the residuals of the data points compared to this calibration curve a plotted.

Cs resonance, and the wavelength of a different well-known laser were used. From the least square fit with a 3rd degree polynomial, the parameters for conversion from pixels to wavelength were extracted (see Fig.10). For the wavelengths-range where most features in our transmission spectroscopy measurements are located, the calibration leads to subnm precision.

5.7 Fluorescence

To get better insight into the level structure of the trapped Rb and Cs atoms, their fluorescence after excitation at a specific wavelength can be studied. To do this, a laser that is relatively easy to scan is needed. For these studies a Ti:Sa femtosecond laser was available. Its relatively high width of 10 nm limits however the resolution of the fluorescence scan quite a bit.
The light emitted by the crystal during excitation with the Ti:Sa laser is afterwards collected in a lens mounted in the innermost shielding (see f in fig.4). Afterwards, the light is collimated into an *Ando AQ-6310c optical spectrum analyser*. It enables recordings between 350 nm and 1750 nm at a resolution of 5 nm.[35]

6 Experimental Results

6.1 Absorption spectra of Cs doped Ar crystals

Cs has been successfully deposited at temperatures between 8 K and 14 kelvin (see fig. 11 and fig. 12).
Comparing the measured spectra, it becomes clear that there are six dominant lines visible and that these lines tend to broaden in warmer deposits. From the plots in fig. 12, it becomes however also clear that two spectra at the same temperature can still differ quite

[35]Settings with higher resolutions, but less sensitivity, are also possible.

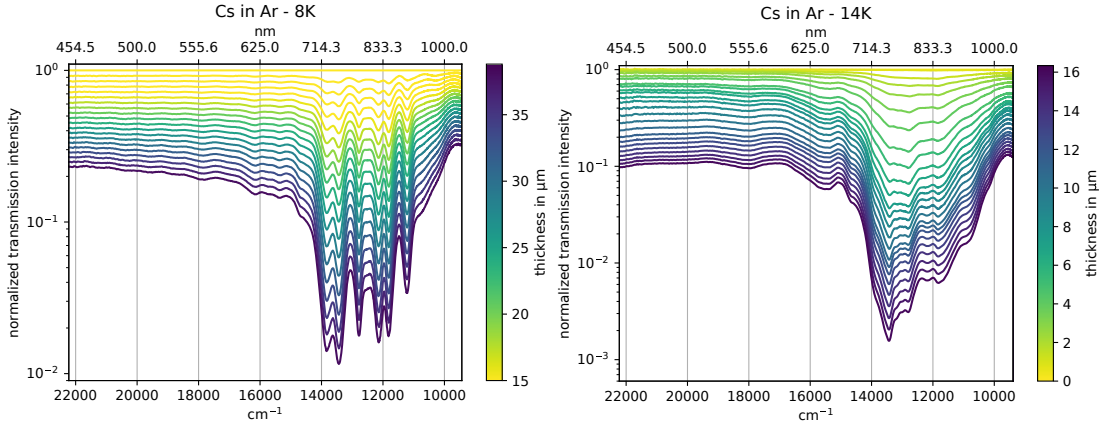

Figure 11: Cs deposits at 8 K and 14 K. During the simultaneous deposition of Ar and Cs, the sample was irradiated with light so that absorption spectra could be taken every minute. All these spectra were then normalized through the first one, which has been taken before any Cs was deposited.

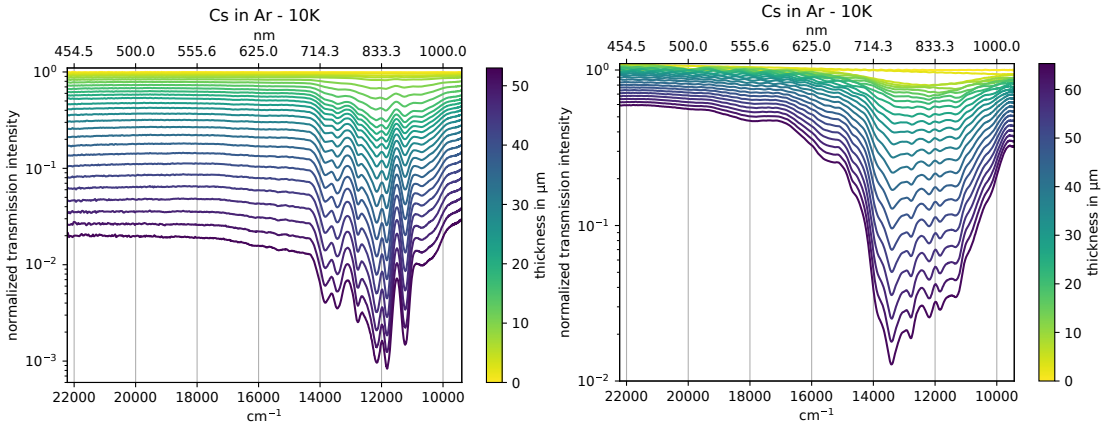

Figure 12: Spectra taken during two different deposits at 10K. Even though the temperature has been the same, both results differ quite a lot.

a lot. This could be due to different deposition rates of Ar and Cs or due to pollutions that influence the crystal structure. Because of clogging in the Cs-dispensers, pollution issues, and difficulties in controlling the Ar flow (see sec. 7), it has not yet been possible to produce multiple spectra under the exact same conditions

One other way to measure the temperature behavior without this difficulty can be achieved by carefully heating and cooling an already formed sample. Such a measure-

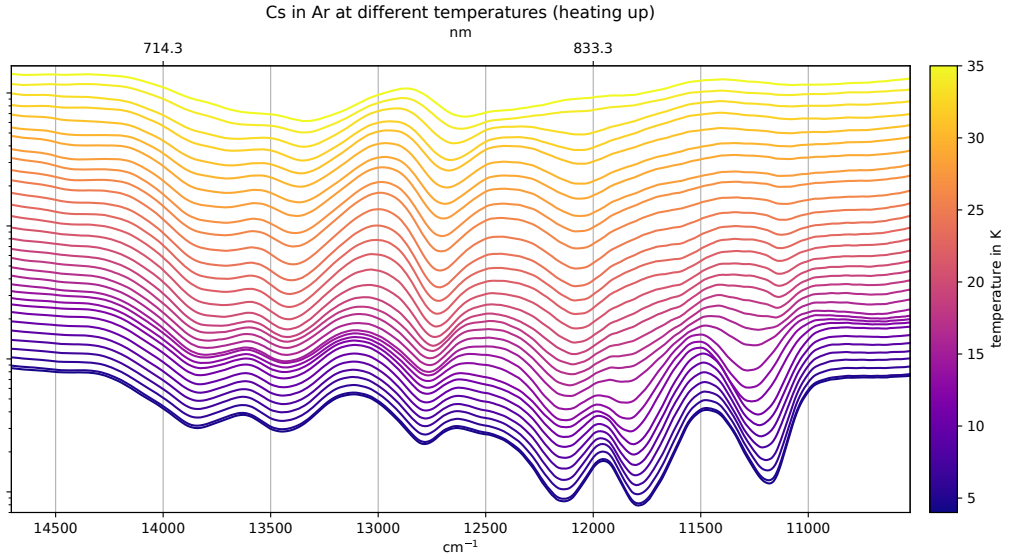

Figure 13: After the sample from fig. 12 *left* was deposited, it has been cooled down to $4.5\,\mathrm{K}$ and afterwards slowly heated. The spectra were normalized through the initial transmission spectrum before the deposit. For better visual clarity, all the curves were horizontally shifted apart from each other, making the y-scale arbitrary.

ment can be seen in fig. 13. In it, one can see that the three left resonances have quite regular wavelengths dependencies with temperature, while the three right ones merge in and shift quite a lot. This data can be used in future studies to compare it to theoretical predictions for the different possible trapping-site symmetries (see sec. 4).

6.1.1 Interpretation of the Cs spectra

In the measured spectra of Cs in Ar, there are six dominant lines visible. In gaseous Cs, there are only two dominant lines[36]. Namely, the $6^2S_{1/2} \rightarrow 6^2P_{1/2}$ and the $6^2S_{1/2} \rightarrow 6^2P_{3/2}$ transition.

When comparing all the data on Cs in Ar, one pattern seems to emerge: The spectra probably consist of two pairs of three peaks. In each triplet, there are two close peaks followed by a third one farther away. The same can be seen for Rb in Ar (fig. 15), only with the difference, that there is a third broadened triplet at lower wavelengths. This multiplicity of the same structure could be explained by multiple types of trapping sites (in this case 2) inhabiting the crystal at once. This interpretation has already been sug-

[36] if the hyperfine structure can not be resolved.

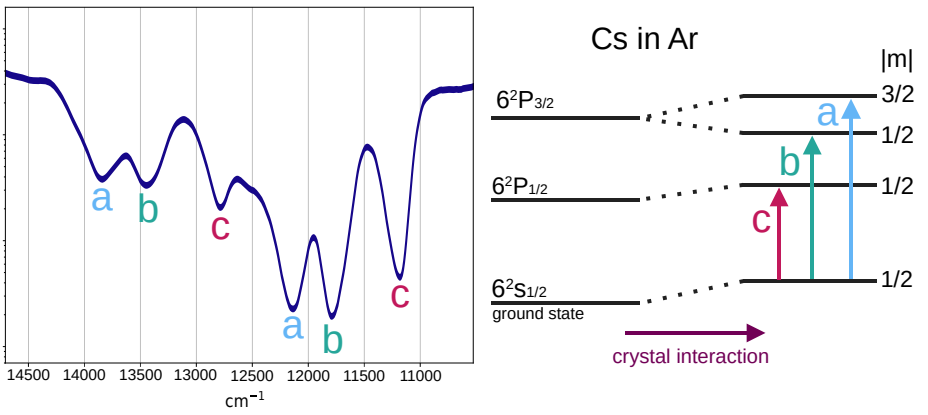

Figure 14: Interpretation of the measured spectrum (*left*) trough the level structure of Cs in Ar (*right*). the crystal interaction lifts the degeneracy in the absolute value of the magnetic quantum number m. The doubling of the triplet is understood as two Cs trapping sites with different energy shifts being present at the same time.

gested in 1968 by Kupferman Pipkin [68] in their study of Rb doped Ar matrices.

Why a doublet in gas phase, becomes a triplet in the matrix, can be understood from the degeneracy of the states. The stark shift, which is induced in the Cs atoms by the crystal field of the surrounding Ar matrix, shifts states according to the absolute value of the magnetic quantum number |m|. Therefore $6^2S_{1/2}$ and $6^2P_{1/2}$ get only shifted, while $6^2P_{3/2}$ splits up in two. This leads to three possible transitions (see fig.14).

Both these effects together would explain the observed spectra.

6.2 Fluorescence

To implement a fluorescence measurement, the Cs dispenser was exchanged for Rb. For the fluorescence of Rb in Ar previous measurements by the group of T. Momose exist [69][37]. This made it easier to optimize the setup for a signal. The absorption spectra taken during the Rb deposit can be seen in fig.15.
With the experience gathered from this measurement, future collecting of fluorescence spectra of Cs in Ar should become much easier. There do not exist any data on this specific system in the literature yet.

To record fluorescence spectra, the excitation laser was tuned to the desired wavelength (680 nm to 900 nm in steps of 10 nm). Afterwards, its power was adjusted to a

[37] A new measurement was also very recently published in June 2022 [52].

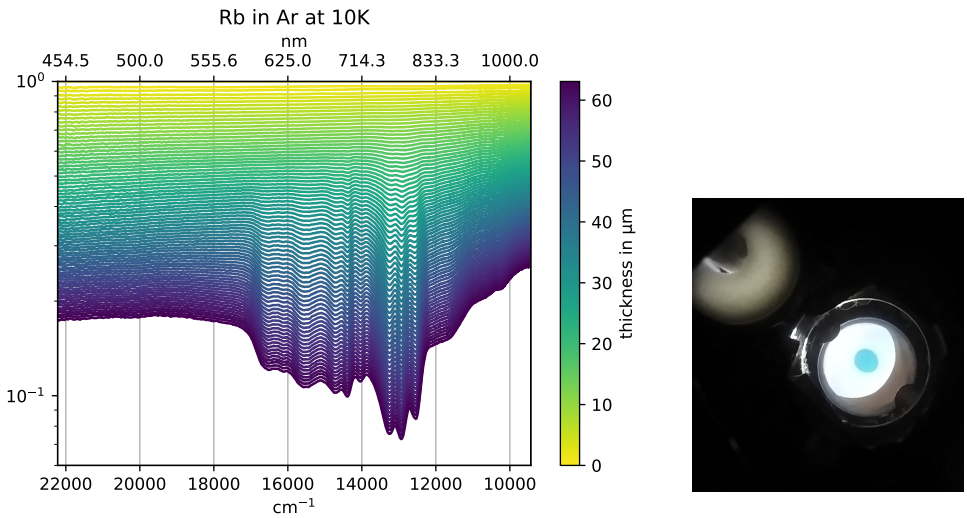

Figure 15: *left:* Deposit of Rb in Ar. This crystal was used for all of the following studies on Rb. *right:* photograph of the Rb doped Ar crystal. The thick Ar layer scatters incoming light and therefore appears white. The Rb atoms absorb mostly red wavelengths which makes them appear blue.

common value $0.67\,\mathrm{mW}$ for all scans. only after the laser's wavelength and power was set, the path to the sample was unblocked to start a measurement. The spectrum analyser then collected light for 5 min. The individual spectra, that were measured this way were later combined into a 2D map by plotting excitation against emission wavelength in fig.16.

6.2.1 Analysis of the Rb flourescence spectrum

Comparing the intensity over excitation wavelength in fig 16 with the previously measured absorption spectrum shows quite similar behaviour as one would expect. The emitted light at $\sim$800 nm however is much brighter than everywhere else. The emission wavelength is also not linear correlated with the absorption wavelength, but instead, most of the emission occurs at $\sim$800 nm too. This suggests that deexcitation mainly occurs at the wavelength previously identified with the $6^2P_{1/2} \rightarrow 6^2S_{1/2}$ transition (see sec. 6.1.1).
The fluorescence measurement was repeated on the same sample cooled down to $5\,\mathrm{K}$ (see fig.17). For it, the laser was swept from high to low wavelength (low to high at $10\,\mathrm{K}$). Despite both these changes, there is no noticeable difference between these two measurements.

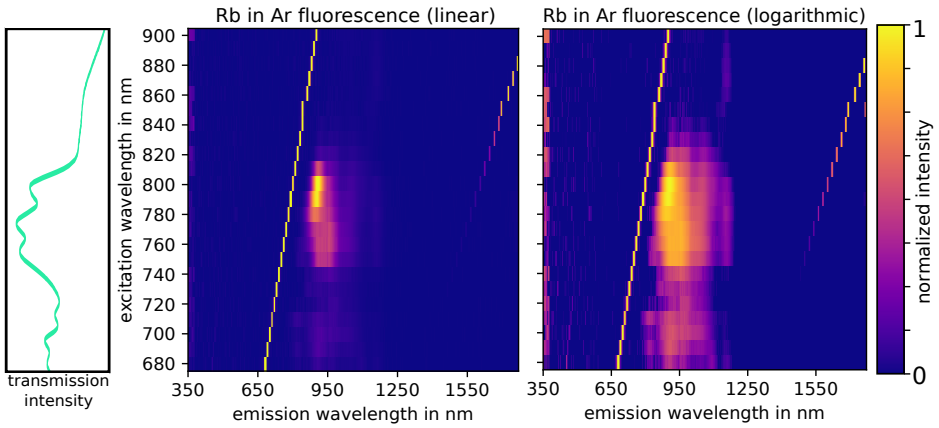

Figure 16: Fluorescence spectra measured in Rb doped Ar at 10K. The spectrum is shown in linear (*left*) and logarithmic scale (*right*) In green the measured absorption spectrum for the different excitation wavelengths is plotted.

In the Fluorescence spectra, there is a narrow line where excitation and emission coincide. It is created by scattering off the excitation laser and therefore just an artifact of the measurement. The same goes for the second narrow line at the top right corner of the pictures. it likely originates from an higher order reflection in the grating of the spectrum analyzer.

6.3 Bleaching

In previous studies by the Weinstein group [64][65], an effect termed 'bleaching' was observed in matrix isolation spectroscopy of alkali metals: After absorbing high-intensity light, the system does not return quickly to its initial state again under the emission of light, but instead the absorption spectrum changes long-term. This non-reversibility can be quite problematic as it prohibits cycling the same transition over long periods of time. This memory effect can also hinder the reproducibility of measurements.

6.3.1 Absorption map of Rb in Ar

A study of this bleaching effect was performed in Rb during the fluorescence measurement. For this, absorption spectra were taken before and after the 5 min irradiation with the laser. The resulting ratios are plotted against the excitation wavelengths in fig 18.
The highest intensity feature in the resulting 2D-map occurs around the line where excitation- and absorption-wavelength coincide[38]. In the 10 K measurement, going from low to high

[38]The bright horizontal feature around 860 nm in the 5K measurement probably originates from modified alignment of the absorption detection during the measurement. It lead to globally increased/decreased ratios.

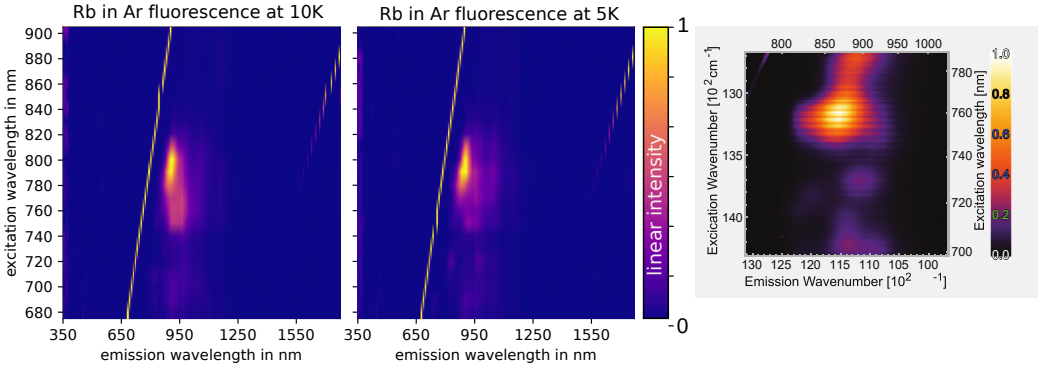

Figure 17: Fluorescence spectra measured in Rb doped Ar at 10K (*left*) and 5K (*center*). For comparison, the fluorescence spectrum for Rb in Ar measured by I. Gerhardt, K. Sin and T. Momose [69] is plotted (*right*).

absorption wavelengths, there is a decrease in intensity followed by an increase, while at the 5 K measurement this order is reversed. This feature looks to be a temperature-dependent effect, but more likely it is just a relict of the way the measurement has been performed. For the 10 K measurement, the excitation laser was swept from low to high wavelengths. That way at any fluorescence measurement, the spectrum is still recovering from the last excitation at 10 nm lower wavelengths. At the same time, however, it gets depopulated at the current excitation wavelength. For the 5 K-scan, the excitation laser was swept from high to low wavelengths. This explains the more or less reversed pattern.

These slow processes which lead to a memory effect, make it hard to gather other information on the interplay of excitations at different resonances. There is some indication in the spectra though that excitations above 850 nm lead to improvement of the high wavelength triplet.

6.3.2 Relaxation time after irradiation

To reduce this kind of effect in a future measurement, it is of interest to measure the time it takes for the spectrum to return to its initial state after an excitation. Therefore, in another measurement on the Rb doped Ar sample, the relaxation behaviour after excitation at 780 nm/0.67 mW for 5 min was recorded. The results of this measurement are shown in fig. 19.

From the measured spectra, it becomes clear, that the system does not return to its initial state over time. Instead, it asymptotically approaches a modified spectrum. This suggests that the irradiation has changed the crystal structure permanently. This could occur by Rb atoms moving out of trapping sites as has been suggested in [70]. It should

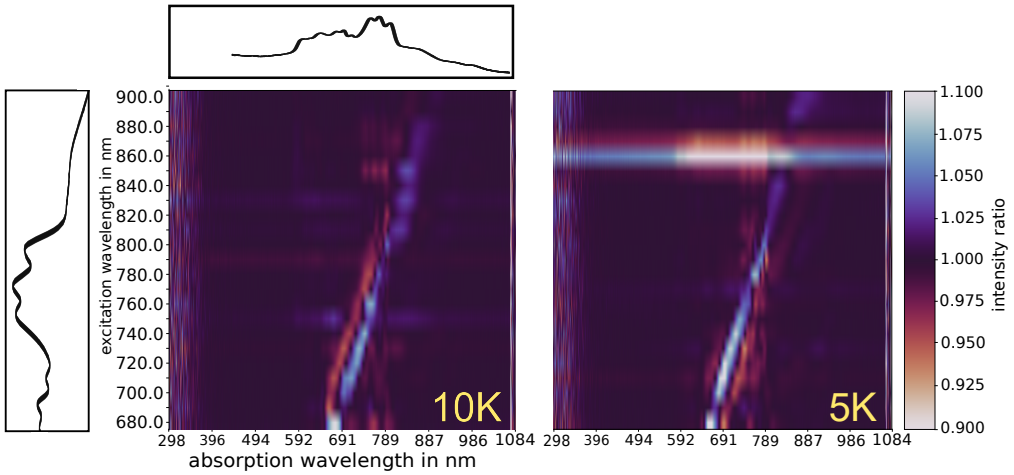

Figure 18: Ratios of absorption spectra after/before irradiation with a laser. The data for the left figure was recorded at $10\,\mathrm{K}$ and the right at $5\,\mathrm{K}$. Blue coloring indicates that the absorption peak has reduced in depths, while red coloring indicates an increase. Additionally, the initial absorption spectrum of Rb in Ar (see fig.15) is plotted against excitation and absorption wavelengths (top and left).

be noted that during the relaxation time, the sample was still irradiated by the lamp. This might have an influence on the relaxation time according to [70].

To avoid artifacts from these slow relaxation processes in the future, the $1/e$-time of the occurring decays has been extracted from fig.19. This was done by comparing the number of counts at the excitation wavelength ($780\,\mathrm{nm}$) over time. The results can be seen in fig 20. The data points have been fitted with exponential decays. This model does not describe behavior at small times well but fits the observations for longer durations. 1/e times of $\tau_{10\,\mathrm{K}} = 5\,\mathrm{min}$ and $\tau_{5\,\mathrm{K}} = 7.7\,\mathrm{min}$ have been extracted from the fits. This gives an idea about optimal waiting times between scans. This should help to redo a measurement similar to the one in fig. 18, but with reduced artifacts around the excitation wavelength.

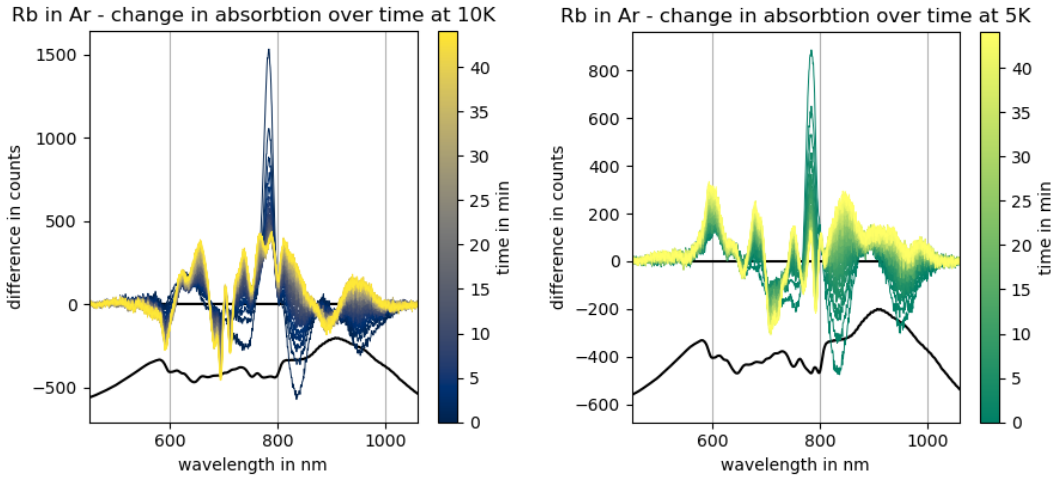

Figure 19: Change in the absorption spectrum of Rb in Ar after being irradiated for 5 min at 780 nm/0.67 mW. The left graph shows the measurement at 10 K and the right one at 5 K. The zero-line in both plots refers to the spectrum before irradiation with the laser. Below both plots, the shape of the absorption spectra at the respective temperature is drawn to visualize where the Rb resonances are located.

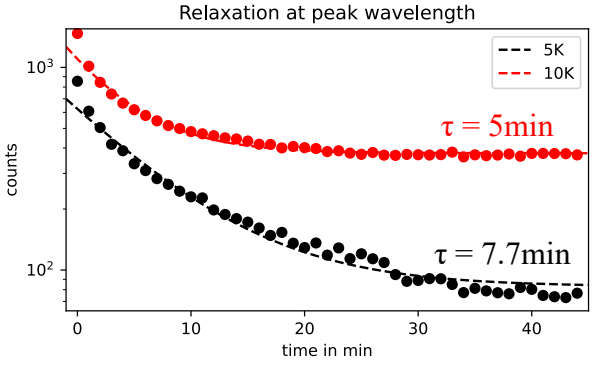

Figure 20: Relaxation behaviour of the spectra in fig.19 at 780 nm. The experimental data (dots) has been fitted with an exponential to obtain the 1/e time τ of these processes.

7 Pollution-issues in the setup

During the whole duration of this project, experiments were plagued by different kinds of pollution arising in the setup at cryogenic temperatures. These required most times to heat the setup to ambient temperature again ($\sim 12\,\mathrm{h}$), which in total cost a large amount of time.
In this section, an overview of the pollution issues is given and it is discussed how these were attempted to be solved.

7.1 Pollution of the Cs source

In the beginning, the experiment utilized a dispenser similar to previous experiments by the Weinberg group [65]. In these, the Ar gas is directly channeled through the alkali oven. For the current experiment, however, it turned out to be much more convenient to separate the noble gas supply from the Alkali oven (see fig. 5 and fig. 4). This made it easier to identify the origins of pollution problems that arose. Additionally, this avoids the issues of Ar freezing in the oven and blocking it (or in reverse condensed Cs blocking the Ar)[39].

When starting this thesis project, no Cs flux from the oven has been observed yet. After opening the oven however it became clear that a lot of Cs got released causing black brittle pollution inside the dispenser. The problem has likely been caused by the released Cs condensing on the inside of the tube of the dispenser. To avoid the same issue in the future, an additional heater was added to the Cs dispenser, and a temperature sensor on the tube exiting it. With that, it has been possible to heat the tube above Cs melting temperature (29° C), and this way enables the controlled emission of Cs.

7.2 Pollution of the Ar

The pollution of the Ar caused problems for much longer than the ones in the Cs dispenser. Often opaque crystals formed on the window. While transparent (probably pure Ar) crystals melted away at $\sim 36\,\mathrm{K}$, opaque crystals only vanished at temperatures above $100\,\mathrm{K}$. Also, attempts of melting this pollution by spraying it with Ar from a heated tube have not been successful. While tests with a residual gas analyzer did not yield clear answers on the composition of this pollution was made off, it is reasonable to assume that the Ar gas got polluted by leaking air and trapped water.
The measurement shown in fig. 21 shows clear indication that water has been present in the setup.

To freeze out possible impurities in the Ar, the gas was directed through a bath of liquid nitrogen. In some trials, there was however so much pollution freezing out in this gas, that the flux was completely stopped.

Future tests on the setup will continue with a new clean Ar bottle, a better-suited valve, and a rebuilt Ar supply line.

[39] Both of these problems have been observed in [65].

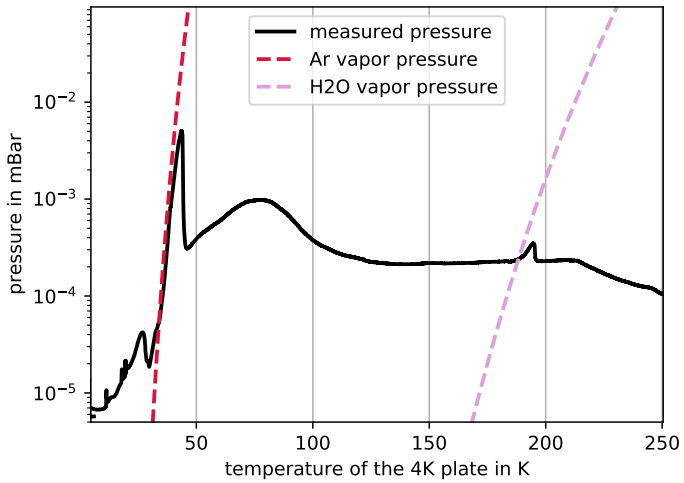

Figure 21: pressure inside the cryostat against the temperature of the '4 K-plate' on which the sample holder is mounted. When some compound melts, this will necessarily lead to an increase in pressure. Literature values from NIST for the vapor pressure of Ar and water are plotted against the measured curve.

8 Axions & ALPs

In these two last sections, two additional searches for beyond SM physics that could be carried out with the present setup (or a similar one) will be discussed.

One special kind of beyond SM particle, that the atomic EDM studies are sensitive to, is the axion, or more general the class of axion-like particles (ALPs). In the following, the motivation behind searches for these particles as well as methods to set constraints onto them in eEDM measurements, are presented.

8.1 The QCD Axion

Experiments show to high precision that CP symmetry is not broken in QCD processes, the Langrangian of the strong interaction, on the other hand, would allow for such a violation. The amount of it can be quantified by a free parameter of the theory, called $\bar{\theta}$. It could take any value between 0 and 2π but is observed to be $<1.5\times10^{-10}$ [27]. This unexplained 'finetuning' is known as the strong CP problem. One possible solution to this problem is given by the Peccei–Quinn theory which explains how the potential of the strong force dynamically gains the observed value at low energy [72][73][74]. The symmetry of this mechanism leads to a new gauge boson, called the (QCD) axion. The theory is not able to make a prediction for its mass or decay constant, but only for the value of their product. According to it, the mass m_a and decay constant f_a, are related

Figure 22: Gravitational lensing in the CL0024+17 galaxy cluster. To achieve the amount of lensing seen in this and similar observations, the existence of dark matter is necessary [71]. Figure credit: NASA/ESA/M J Jee (John Hopkins University)

by $m_a = 5.691(51) \times 10^{15} \left(\frac{\mathrm{eV}^2}{f_a}\right)$ [75].
Axions are popular candidates for dark matter particles. The ranges that are compatible with astronomical observations and simulations, would describe a spread-out Bose gas with small couplings to SM particles. Due to its gravitational pull, this gas would form halos around galaxies and therefore explain the amount of unexplained mass in astronomical observations [76].
Because of its ability to potentially solve two big problems of physics at once and its on the other hand, quite free parameter space, there are numerous experiments all around the world, searching for axions. A review on the topic can be found in [77][76][78].

8.2 ALPs

Beyond the theory of the Peccei–Quinn mechanism, there are also the so-called axionlike particles (ALPs), which as pseudoscalar fields possess, the same couplings as the QCD axion, but not its restriction on a specific decay constant to mass ratio. Particles with such a behaviour come up in numerous beyond SM theories, for example in a lot of string theories [79]. ALPs also share the potential to be the ingredients of dark matter.

Additionally, theories exist in which ALPs are able to explain the observed matter-antimatter asymmetry in the universe. Either by enabling new cosmic objects that could contain the 'missing' antimatter [80] or by showing how ALPs could lead to the Baryon asymmetry in the early universe [81].

8.3 Sensitivity of atomic EDMs to ALPs

There are multiple ways how measurements on eEDMs are sensitive to the large parameter space of axion-like particles, including the QCD axion itself:

(a) In [82], Y. Stadnik, V. Dzuba, and V. Flambaum describe how the axion could act as a CP violating force carrier in electron-electron interaction V_{ee} and electron-

nucleon interaction V_{ne}. This interaction can be modeled with the following potential[40]:

$$V_{12}(r) = i\frac{g_1^p g_2^s}{4\pi}\frac{e^{-m_a r}}{r}\gamma^0\gamma_5 \tag{28}$$

were g_1^s is a constant for the scalar and g_2^p for the pseudoscalar coupling between axions and electrons/nucleons. Such a coupling between nucleons and electrons would have a similar effect as C_S in (11) and could be evaluated analogously. Any measurement of the eEDM, therefore automatically probes for axions that couple to electrons. In this framework, ALPs appear as virtual force carriers and the assumption that they make up all of the observed dark matter is therefore not necessary.

(b) As quasifree, light Bosons, ALPs would form a condensate[41] of states with high occupation numbers[84]. This in turn means that their density oscillates like the free particle solutions to the Klein-Gordon equation [46]. As derived in [85], this would, trough coupling of opposite parity states, induce an oscillating EDM in alkali atoms of strength:

$$d_a = -e\,\frac{\sqrt{2\rho_{\text{DM}}}\,m_a\alpha_s}{\alpha\,f_a}\,\sin\left(m_a t\right) \tag{29}$$

Here $\rho_{\text{DM}} \sim 0.3$–$0.45\,\text{GeV/cm}^3$[86] is the dark matter density around earth, α_s is the static scalar polarizability of the atom, α is the fine structure constant, m_a is the unknown axion mass and f_a the unknown axion decay constant. Here it is assumed that a single ALP field makes up all of the observed dark matter.

(c) In more exotic models ([80],[87],[88]), ALP densities are not evenly distributed or ALPs with different couplings inhabit different regions of space. These structures are expected to cross earth from time to time. As previously explained this would directly induce atomic EDMs as their value would also be influenced by these varying densities. That way the Bursts in ALP density predicted in these exotic models could be measurable as bursts in d_a [89].

Atomic EDM measurements are automatically sensitive to couplings with ALPs of the above-discussed type (a). It is just necessary to calculate ALP bounds from the results afterward as it was done in [82]. This even excludes a region in the space of possible QCD axions.
To enable sensitivity to type (b) ALPs, it is necessary to perform a time-sensitive evaluation of the measured data as it was done for the JILA HfF+ EDM measurement in [90] or as it is attempted in the axion detector project CASPEr [46]. The duration of a single run compared to the whole measurement campaign gives the addressable mass range of the ALP masses.
To additionally include sensitivity to ALPs of type (c), the information about the experiment's location (in reference to the CMB) is also helpful. Because the expected signatures

[40]For simplicity, the equations in this section are given in natural units: $\hbar = c = 4\pi\varepsilon_0 = 1$
[41]In some theories this condensate is even a Bose-Einstein condensate [83].

are sudden nonperiodic modulations, it will be hard to distinguish them from statistical fluctuations. Therefore a measurement scheme similar to one of the GNOME collaboration [91] has been suggested [89]. In GNOME, magnetometers on different continents form a network. Comparing their measurements makes it possible to neglect false positives that were only seen in a single experiment. Additionally in case of a real event, one could gather more information like their direction of origin.

In total, one can conclude that axion searches are well motivated as experimental bounds on them put similar to eEDM searches and CPT-violation experiments valuable bounds on the parameter spaces of beyond SM theories. Because of their property to create oscillating eEDMs, it is therefore wise to take data in future experiments in a way that enables besides the actual eEDM measurement a time-dependent evaluation of the measured signals.

9 The Nuclear Anapole Moment

The anapole moment already previously appeared in the Lagrangian of the possible interactions of a spin-½ Dirac-Fermion (1). This anapole moment of the electron however is believed to be not a physical measurable quantity as it is not gauge-invariant [92][10][42]. This however is not true anymore for heavy composited particles. So even though the anapole moment of electrons, neutrons, or protons can not be meaningfully defined, the **nuclear** anapole moment is a physical quantity. To this day, only one successful measurement of the nuclear anapole moment has been performed in 1997 on a beam of Cs atoms [94]. A confirmation of this result, as well as measurements on other species, are of great interest as they provide insight into intranuclear couplings and give a valuable test of the weak force at low energies [95]. These could test models which predict additional weak gauge Bosons[43]. While high energy experiments like the LEP provided very stringent tests on the electroweak theory at high energies, its validity at low energies is only poorly probed yet [98][99]. All this indicates that further measurements of anapole moments are needed.

In the following, a small overview of the theory behind the nuclear anapole moment (NAM) is given as well as a discussion of how it could be measured in atoms trapped in a cryogenic matrix.

9.1 Definition of the anapole moment

An electromagnetic multipole expansion in the far field makes it possible to describe any charge and current distribution as a sum of electrostatic and magnetostatic multipoles. In the near field, this is however generally not sufficient anymore and the addition of toroidal multipoles is required [100][101][10]. The lowest order of toroidal moments gives rise to the so-called anapole moment **a**. It is defined in the following way: A current

[42] [93] on the other hand claims that for leptons a gauge independent formulation is possible

[43] [96] even suggests that the anomalies seen in previous parity violation studies in Cs could be linked to the recently arising discrepancy in the W-Boson mass[97].

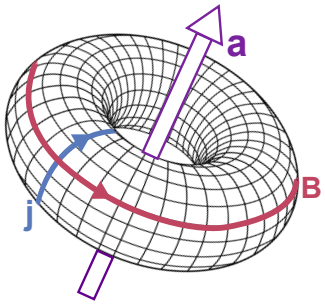

Figure 23: When a current j flows in a toroidal coil, an internal magnetic field B is created. This configuration correspond to an anapole moment **a**.

$j(r)$ creates an anapole of

$$\mathbf{a} = \int d^3r\, \boldsymbol{r}^2 \boldsymbol{j}(\boldsymbol{r}) \tag{30}$$

It can be understood as a toroidal magnetic field directed orthogonal to a like the one that is generated when a current flows through a toroidal coil (see fig. 23).

9.1.1 Anapole moments in the standard model

Anapole moments are odd under parity P, but even under time reversal T. Because the electromagnetic and the strong interaction do not violate parity, it becomes intuitively clear that anapoles in the standard model can only originate from the weak force. In the case of the nuclear anapole moment (NAM), this is the weak interaction between nucleons. The most significant contribution does not come from direct interactions between nucleons through Z^0, but is instead mediated by weak interactions with virtual mesons that possess a much farther reach than Z^0 alone [102] (see fig. 24).

The NAM **a** can be calculated from the weak current inside the nucleus. A calculation inside the nuclear shell model leads to[103]:

$$\mathbf{a} = \frac{G_F}{\sqrt{2}e} \frac{K\boldsymbol{I}}{I(I+1)} \kappa_{\mathbf{a}} \tag{31}$$

G_F is the Fermi constant, **I** the nuclear spin, and $K = (I + \frac{1}{2}) \cdot (-1)^{I+\frac{1}{2}-l}$ with the nuclear angular momentum l. $\kappa_{\mathbf{a}}$ is a dimensionless constant that quantifies the strength and sign of the anapole. The goal of experimental searches is to measure its value. It is approximately given by $\kappa_{\mathbf{a}} = \alpha A^{2/3}$ [104]. Here α is the fine structure constant and A the nucleus mass number.
The anapole moment creates a parity-violating electromagnetic vector potential inside the nucleus[103]:

$$\boldsymbol{A}(\boldsymbol{r}) = \mathbf{a}\rho(\boldsymbol{r}) \tag{32}$$

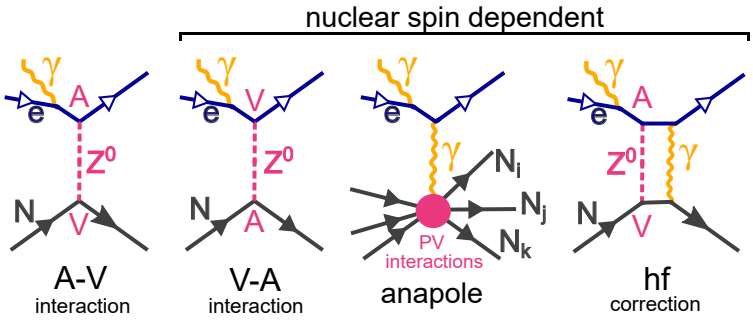

Figure 24: Leading order Feynman diagrams of the most significant parity violating electron-nucleon interactions. From left to right: nucleus-vector to electron-axial-vector (A-V) weak neutral current, nucleus-axial-vector to electron-vector (V-A) weak neutral current, Nuclear anapole moment to electron electromagnetic interaction, weak correction to the hyperfine (hf) coupling.

with $\rho(\boldsymbol{r})$ being the nuclear weak-charge distribution[44].
According to the Dirac equation, electrons couple through vector potentials according to

$$V = e\boldsymbol{\alpha} \cdot \boldsymbol{A} \tag{33}$$

Combining (31), (32) and (33) yields the relativistic interaction potential for electrons in the field of a NAM:

$$V_{\text{NAM}}^{\text{rel}} = \frac{G_F}{\sqrt{2}} \frac{K\boldsymbol{I} \cdot \boldsymbol{\alpha}}{I(I+1)} \kappa_{\mathbf{a}} \rho(\boldsymbol{r}) \equiv \varkappa_{\mathbf{a}} \boldsymbol{I} \cdot \boldsymbol{\alpha} \rho(\boldsymbol{r}) \tag{34}$$

9.1.2 Other nuclear spin dependent interactions

A more general treatment of parity-violating electron-nucleus interactions shows that $H_{\text{NAM}}^{\text{rel}}$ is not the only nuclear spin-dependent (NSD) term. The axial vector - vector coupling $\varkappa_{\text{a-v}}$ and the weak force correction to the hyperfine interaction $\varkappa_{\text{hf}}$ are proportional to $\boldsymbol{I} \cdot \boldsymbol{\alpha}$ as well (see fig. 24). A measurement will therefore be sensitive to the combined potential of these three:

$$V_{\text{NSD}} = (\varkappa_{\text{a-v}} + \varkappa_{\mathbf{a}} + \varkappa_{\text{hf}}) (\boldsymbol{I} \cdot \boldsymbol{\alpha}) \rho(\boldsymbol{r}) = \varkappa_I (\boldsymbol{I} \cdot \boldsymbol{\alpha}) \rho(\boldsymbol{r}) \tag{35}$$

Usually, the hyperfine component is suppressed compared to the other two and beyond that, its value can be calculated with good precision [105]. The contribution of the other two components depends on the nuclear structure [106]. For Cs and Rb the anapole contributions are dominating [107].

[44] normalized to $\int d\boldsymbol{x} \rho = 1$

The effect of V_{NSD} will mix states of different parity inside the atom. Because of that, transitions between states that are forbidden due to vanishing dipole transition elements $\langle\psi|e\boldsymbol{r}|\psi\rangle$, become possible[45]. By measuring the transition amplitude of such a parity-forbidden transition (e.g. $6s \rightarrow 7s$-transition in Cs), one can therefore determine the size of $\varkappa_I$.

9.1.3 Nuclear Spin Independent effect

There is however an additional parity violating interaction. This interaction (in leading order) is given by the A-V exchange of a Z^0-Boson (see fig. 24). It is nuclear spin-independent (NSI) and given by the relativistic interaction potential [108]:

$$V_{\text{NSI}} = -\frac{G_F}{\sqrt{2}}\frac{Q_W}{2}\rho(\boldsymbol{r})\gamma_5 \tag{36}$$

where Q_W is the weak charge. This effect will also be able to mix states of different parity, but around 100 times stronger than the NSD interactions. This contribution provides therefore one of the major difficulties in measurements of $\varkappa_I$. To disentangle nuclear dependent and independent effects, one has to make use of the fact that only the NSD effects depend on the nuclear angular momentum $\boldsymbol{I}$. It is therefore possible to measure parity-forbidden transitions involving different hyperfine levels to get access to the small V_{NSD} contribution. This is also what has been done in the only successful anapole moment measurement [94]. Other similar measurements were not able to reach the extreme precision that is necessary to obtain a statistically significant result from hyperfine-dependent differences in the transition amplitude [109][110].

In the following section, a different method is explained that would yield results directly proportional to NSD effects without influence of the NSI interaction.

9.2 NAM of atoms in crystalline matrices

In [111] M.A. Bouchiat and C. Bouchiat, who are pioneers in the experimental and theoretical exploration of parity violation in atoms, provide the theory behind a Stark effect that arises in crystalline matrices due to the NAM. This effect could be of interest for future measurements in the setup presented in this thesis.

The authors argue that even though in a transition between two states with different principal quantum number n, both V_{NSD} and V_{NSI} contribute, inside a manifold with the same n, the transition amplitude will be solely dependent on V_{NSD}. Inside a free atom, there will however be no energy $\Delta\mathcal{E}$ splitting from parity violating effects. And as M.A. Bouchiat and C. Bouchiat show, even under the application of an external (laboratory) electric field E and magnetic field B, $\Delta\mathcal{E}$ will still be zero. Similar to the eEDM in section 2.3.4 that required the breaking of symmetry under the parity transform P to create an energy shift, for the anapole, breaking the rotational symmetry around the axis $\hat{u} = \frac{\boldsymbol{E}\times\boldsymbol{B}}{|\boldsymbol{E}||\boldsymbol{B}|}$ is required.
This can be achieved by implanting the atoms inside a crystal (like it was done in this project). If the crystal possesses a reduced symmetry with at least one preferred axis $\boldsymbol{n}$, the rotational symmetry around $\hat{u}$ will be broken. In a system like this, the hyperfine

[45] This is analogous to the case of the eEDM shown in (7)

coupling will be anisotropic and given by a 3×3-matrix $\overleftrightarrow{\boldsymbol{A}}$, acting on the electron spin $\boldsymbol{s}$ and nuclear angular momentum $\boldsymbol{I}$ according to $H_{\text{hf}} = \boldsymbol{s}\overleftrightarrow{\boldsymbol{A}}\boldsymbol{I}$. In their calculation, the authors assume a uniaxial crystal. In it, $\overleftrightarrow{\boldsymbol{A}}$ takes the form:

$$\overleftrightarrow{\boldsymbol{A}} = \begin{pmatrix} A_\perp & 0 & 0 \\ 0 & A_\parallel & 0 \\ 0 & 0 & A_\parallel \end{pmatrix} \tag{37}$$

In such an environment, there will be an anapole induced stark shift:

$$\Delta\mathcal{E} = \langle \boldsymbol{E} \cdot \boldsymbol{d}_n \rangle = \langle \boldsymbol{E} \cdot [\varkappa_I \, \widetilde{b}_n \, (\boldsymbol{s} \times \boldsymbol{I})] \rangle \tag{38}$$

$\widetilde{b}_n = b_n/\varkappa_I$ is a constant that is dependent on the atomic system and the principal quantum number n.

Even though the shift occurs for arbitrary (nonzero) magnetic fields, the behavior of the system becomes clearest when $g_s\boldsymbol{B} \ll A_\parallel, A_\perp$ is assumed[46]. Because of the anisotropy, the nucleus will perceive the external magnetic field rotated from its actual direction. Therefore not the nuclear angular momentum I, but instead its rotation into this new frame of reference $\widetilde{I}$ will commute with the Hamiltonian of the system. This makes the z projections of $\boldsymbol{s}$: m_s, and the z-projection of $\widetilde{\boldsymbol{I}}$: $m_{\widetilde{I}}$ good quantum numbers. Under these considerations, the expectation value in (38) can be calculated [111]:

$$\begin{aligned} \Delta\mathcal{E} &= \langle ms, \widetilde{m}_I | \boldsymbol{E} \cdot \boldsymbol{d_n} | ms, \widetilde{m}_I \rangle = \langle ms, \widetilde{m}_I | \boldsymbol{E} \cdot [\varkappa_I \, \widetilde{b}_n \, (\boldsymbol{s} \times \boldsymbol{I})] | ms, \widetilde{m}_I \rangle \\ &= -2\varkappa_I \, \widetilde{b}_n m_s m_I \, \frac{(\boldsymbol{n} \cdot \boldsymbol{B}) \, (\boldsymbol{n} \cdot (\boldsymbol{E} \times \boldsymbol{B}))}{\boldsymbol{B}^2} \, \frac{A_\parallel - A_\perp}{A_\parallel + A_\perp} \end{aligned} \tag{39}$$

9.2.1 Possible measurements of this energy shift

An anapole measurement with the method presented here has never been attempted. In the following, some thoughts on performing such an experiment in the future are presented:

The application of an external magnetic field will necessarily lead to a Zeeman shift as well. The energy shift due to the anapole (39) however does not depend on the magnitude of $\boldsymbol{B}$ and even stays invariant under $\boldsymbol{B} \to -\boldsymbol{B}$. By varying $\boldsymbol{B}$ it should therefore be possible to differentiate between the Zeeman and the parity-violating Stark splitting with good precision.

For a first measurement, Cs is advantageous because of the numerous studies on P-violation which were previously carried out already, and the high precision in calculations of this system. This could also provide an independent test of the 1997 measurement which to this day is not in complete agreement with other measurements and theoretical predictions[99].

[46] In this situation nuclear angular momentum and electron spin couple stronger to the magnetic field than to each other (hyperfine Paschen-Back-regime)

But for developing good models, it is important to not base all calculations on just a single atomic species. Rb provides a good candidate for an additional system. As an alkali metal, atomic calculations are possible to perform for it with relatively good precision. Its mass is also still sufficient to make the anapole contribution to $\varkappa_I$ large enough [112]. In [107] calculations for the anapole constants $\kappa_{\mathbf{a}}$ of Rb were performed. Their values are in the same order of magnitude as Cs and they have the experimentally useful property that the signs for the two naturally occurring isotopes ^{85}Rb and ^{87}Rb are opposite from each other.
Also, potassium, which would be easily implemented in the experimental apparatus presented in this thesis, has previously been discussed as a good system for anapole measurements [113].

Beyond that, the method of matrix isolation spectroscopy might be able to study Ba^+ and Ra^+ ions[47, 48]. Due to their single valence electron theoretical techniques similar to alkali atoms can be used, while their positive charge binds the electron even closer causing greater overlap with the nucleus and therefore enhanced sensitivities to the local interaction potential V_{NSD}.

A completely different scheme to measure the NAM in solids is proposed in [22] and [116]. Analogously to magnetometry measurements of the eEDM-induced linear $\boldsymbol{E}$-$\boldsymbol{B}$ coupling in sec. 3.2, they propose to measure the anapole-induced orthogonal $\boldsymbol{E}$-$\boldsymbol{B}$ coupling with the same method.

9.3 Measurement in a poly-crystal

The cryogenic matrix in this experiment is likely to be poly-crystalline. Therefore in the following, it should be investigated how the anapole-induced energy shift $\Delta\mathcal{E}$ can still be measured even if the direction of local anisotropies n are randomly distributed across the crystal.
For that, I will define the direction of the magnetic field $\boldsymbol{B}$ as $\boldsymbol{z}$ and choose the electric field $\boldsymbol{E}$ in $\boldsymbol{y}$-direction[49]. The direction of $\boldsymbol{n}$ can then be expressed in this coordinate system with the spherical coordinates ϕ and θ. In this coordinate system, the energy shift from (39) becomes :

$$\begin{aligned}\Delta\mathcal{E} &= -2\varkappa_I\,\widetilde{b}_n m_s m_I\,\frac{(B\cos\theta)\,(E\,B\sin\theta\cos\phi)}{B^2}\,\frac{A_\parallel - A_\perp}{A_\parallel + A_\perp} \\ &= -2\varkappa_I\,\widetilde{b}_n m_s m_I\,E\,\frac{A_\parallel - A_\perp}{A_\parallel + A_\perp}\,\tfrac{1}{2}\cos(\phi)\sin(2\,\theta) \equiv X\cdot\tfrac{1}{2}\cos(\phi)\sin(2\,\theta)\end{aligned} \tag{40}$$

[47] The possibility of doping a Xe matrix with Ba^+ has already been demonstrated by the nEXO collaboration [114].

[48] In [115] it is argued that Ra^+ has quite advantageous properties for an anapole measurement. Due to its valence neutron, ^{226}Ra provides information complementary to ^{133}Cs, which has a valence proton instead.

[49] $\Delta\mathcal{E}$ is maximal for $\boldsymbol{B}$ orthogonal to $\boldsymbol{E}$

Now the distribution of energy shift can be determined by a quick Monte Carlo simulation. Under the assumption of spherically uniformly distributed values of ϕ and θ[50], the histogram in fig. 25 was created. From fig. 25 it becomes clear that instead of an energy

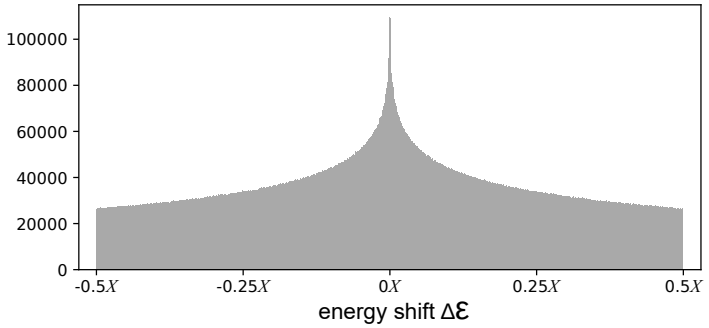

Figure 25: Monte Carlo histogram of the distribution of anapole-induced energy shifts in a poly-crystal. 10^7 random directions of $\boldsymbol{n}$ with uniform probability were used. X is defined according to (40).

shift, there will be a line-broadening instead. Because the histogram is symmetric under $X \to -X$ it will also be invariant under $\boldsymbol{E} \to -\boldsymbol{E}$. The magnitude of E however determines the amount of broadening. Therefore even though it won't be possible anymore to measure the difference in energy shifts between opposite configurations of $\boldsymbol{E}$, it should still be possible to measure the difference in line-widths between the transitions with and without applied $\boldsymbol{E}$-field. Also, the slow decaying flanks of the here calculated distribution should be beneficial for such a measurement.

9.3.1 Sensitivities to axions in an anapole measurement

The possible effect of axions on anapoles has been noted in literature [85][117], but to my knowledge, the size of this effect has not yet been evaluated. Because this is however of interest in the context of a possible future anapole experiment, it should be done here:

As previously discussed in section 8.3, oscillating dark matter ALPs might mix opposite parity states of atomic levels. In [85] it is shown how mixing of opposite parity states inside a nucleus by the same effect, would lead to oscillating anapole moments:

$$\mathbf{a}(t) = \frac{4}{3}\frac{\sqrt{2\rho_{\text{DM}}}\,\pi r_0^3}{e\,g_N f_a}\,\frac{K\boldsymbol{I}}{I(I+1)}\kappa_{\mathbf{a}}\sin\left(m_a t\right) \tag{41}$$

With $r_0 = 1.25\,\text{fm}$ and g_N being a coupling constant for the valence nucleon (in case of Cs, the valence nucleon is a proton and $g_N = g_p = 4.5$ [118]). Apart from different constants and the time dependency, this equation is completely analogous to (31). That way under the substitution $\varkappa_{\mathbf{a}} \to \varkappa_{\mathbf{a}}\left[1 + k\sin(m_a t)\right]$ with $k = \frac{8}{3}\frac{\sqrt{\rho_{\text{DM}}}\,\pi r_0^3}{G_F\,g_N f_a}$, the previous

[50]To achieve a uniform sampling, one has to use ϕ=2πu and θ=acos(2v-1), with u and v being uniform random values in the interval (0,1).

discussions for a possible measurement remain valid. Calculating k for Cs yields:

$$k \approx 7{\times}10^{-4}\frac{\mathrm{eV}}{f_a} \tag{42}$$

As the axion decay constant is expected to be $\gg 1$ GeV [78], measuring anapole moments to a precision where effects from ALP oscillations become noticeable, seems unrealistic. Especially for the QCD axion, one gets:

$$k_{\text{QCD}} \approx \frac{m_a}{10^{19}eV} \tag{43}$$

The axion masses that one could probe are many orders of magnitude too high to justify assumptions about the assumptions leading to equation (41). Only a dark matter axion field with light masses can form a condensate that leads to the oscillating behavior of EDMs and the anapole.

10 Conclusion

In this thesis, I presented the theory of how new physics beyond the standard model would lead to an electron EDM and how it would express itself in the energy levels of alkali atoms embedded in a cryogenic matrix. Following this, schemes to measure these effects were shortly presented, leading to an understanding of the statistical uncertainties that such an experiment will be limited to and how to suppress them. It is desirable to maximize particle number, decoherence time, and the effective electric field strength. To learn more about systematic uncertainties, on the other hand, previous eEDM searches performed in solids were analyzed. One major source of systematic uncertainties, the magnetoelectric effect, was discussed in more depth to deduce how it could express in the system used for this experiment. It was found that issues arising from this effect can probably be avoided for Cs doped Ar.

After giving an overview of the setup and experimental techniques, the results from different measurements were presented and discussed. During this thesis, Cs and Rb have been successfully implanted into a cryogenic matrix of Ar. The obtained spectra agree with the explanation provided by Kupferman and Pipkin [68]. Namely one likely observes splitting of spectral lines due to different Cs trapping sites and the stark splitting induced by the matrix.

Additionally, fluorescence spectra of Rb and studies of the relaxation time after irradiation with a strong laser were discussed. These results can be helpful for future fluorescence measurement of Cs.

Following this, the issues of pollution in the setup were addressed. These gave a great complication during the whole duration of the project and will hopefully soon get resolved.

In the final two sections, the theory behind two experimental searches distinct from the eEDM was presented: The search for axion dark matter is an endeavor performed by numerous groups around the world. It was explained how eEDM searches can provide sensitivities to these hypothetical particles with only little effort. The second search is the measurement of the nuclear anapole moment in atoms embedded in a cryogenic matrix. It was explained how for a system like the one used in this thesis, this property can

express in a similar way as the eEDM.

In the future, there is a number of studies remaining, before a measurement for the eEDM can be attempted. Specific calculations for Cs in Ar need to be carried out to determine the EDM enhancement factor in this system. Additionally, a conclusion on the shape of the trapping sites of Cs in Ar is needed. For this further experimental studies (magnetic circular dichroism and fluorescence in Cs) will be carried out at Laboratoire Aimé Cotton (LAC) together with theoretical investigations at Centre de recherche sur les Ions, les MAtériaux et la Photonique (CIMAP).
Additionally, a measurement of the decoherence time of the system will be essential in evaluating the feasibility of measuring the EDM of Cs atoms embedded in Ar.

11 Acknowledgements

I want to thank the university of Bonn and the laboratoire Aimé Cotton for enabling me to write this thesis. Also thanks to the ANR and CNRS for financing this thesis project.

I like to thank Thomas Battard, who worked together with me on the EDMMA experiment, and above all Daniel Comparat, who was always a great supervisor with very helpful feedback and discussions. I also want to thank Simon Stellmer for cosupervising this thesis project. Not to forget, thanks to Chloé Malbrunot for organizing the contact to Paris that enabled this all and to Olivier Dulieu, the director of the laboratoire Aimé Cotton.

Finally, I want to thank my parents Martin and Orphea, and my sister Sophia who always supported me through all my studies, and Yuchen who motivated me so much!

Merci Beaucoup!

References

[1] H. Nataraj, B. Sahoo, B. Das, R. Chaudhuri, and D. Mukherjee, "The electron electric dipole moment enhancement factors of rubidium and caesium atoms," in *J.of Phys.: Conference Series*, vol. 80, p. 012050, IOP Publishing, 2007.

[2] Y. Yamaguchi and N. Yamanaka, "Quark level and hadronic contributions to the electric dipole moment of charged leptons in the standard model," *Phys. Rev. D*, vol. 103, no. 1, p. 013001, 2021.

[3] M. Pospelov and A. Ritz, "Ckm benchmarks for electron electric dipole moment experiments," *Phys. Rev. D*, vol. 89, no. 5, p. 056006, 2014.

[4] D. Griffiths, *Introduction to elementary particles - Chapter 10.5.* John Wiley & Sons, 2020.

[5] V. Andreev and N. Hutzler, "Improved limit on the electric dipole moment of the electron," *Nature*, vol. 562, no. 7727, pp. 355–360, 2018.

[6] T. Chupp, P. Fierlinger, M. Ramsey-Musolf, and J. Singh, "Electric dipole moments of atoms, molecules, nuclei, and particles," *Reviews of Modern Phys.*, vol. 91, no. 1, p. 015001, 2019.

[7] A. et al., "Electric dipole moments and the search for new physics," *arXiv preprint arXiv:2203.08103*, 2022.

[8] L. Canetti, M. Drewes, and M. Shaposhnikov, "Matter and antimatter in the universe," *New J.of Phys.*, vol. 14, no. 9, p. 095012, 2012.

[9] A. Czarnecki and W. J. Marciano, *Lepton dipole moments - Chapter 14*, vol. 20. World Scientific, 2010.

[10] W. Haxton and C. Wieman, "Atomic parity nonconservation and nuclear anapole moments," *Collected Papers of Carl Wieman*, vol. 51, p. 209, 2008.

[11] M. E. Peskin, *An introduction to quantum field theory - chapter 6.* CRC press, 2018.

[12] M. D. Schwartz, *Quantum field theory and the standard model.* Cambridge University Press, 2014.

[13] F. Schwabl, "Advanced quantum mechanics; quantenmechanik fuer fortgeschrittene," 1997.

[14] L. Schiff, "Measurability of nuclear electric dipole moments," *Phys. Rev.*, vol. 132, no. 5, p. 2194, 1963.

[15] P. G. H. Sandars, "The electric dipole moment of an atom," *Phys. Lett.*, vol. 14, no. 3, pp. 194–196, 1965.

[16] C.-P. Liu, M. Ramsey-Musolf, W. Haxton, R. Timmermans, and A. Dieperink, "Atomic electric dipole moments: The schiff theorem and its corrections," *Phys. Rev. C*, vol. 76, no. 3, p. 035503, 2007.

[17] E. R. Meyer, J. L. Bohn, and M. P. Deskevich, "Candidate molecular ions for an electron electric dipole moment experiment," *Phys. Rev. A*, vol. 73, no. 6, p. 062108, 2006.

[18] D. A. Steck, "Cesium d line data," 2019.

[19] E. D. Commins, S. B. Ross, D. DeMille, and B. Regan, "Improved experimental limit on the electric dipole moment of the electron," *Phys. Rev. A*, vol. 50, no. 4, p. 2960, 1994.

[20] S. Murthy, D. Krause Jr, Z. Li, and L. Hunter, "New limits on the electron electric dipole moment from cesium," *Phys. Rev. Lett.*, vol. 63, no. 9, p. 965, 1989.

[21] W. B. Cairncross, D. N. Gresh, M. Grau, K. C. Cossel, T. S. Roussy, Y. Ni, Y. Zhou, J. Ye, and E. A. Cornell, "Precision measurement of the electron's electric dipole moment using trapped molecular ions," *Phys. Rev. Lett.*, vol. 119, no. 15, p. 153001, 2017.

[22] S. Lamoreaux, "Solid-state systems for the electron electric dipole moment and other fundamental measurements," *Phys. Rev. A*, vol. 66, no. 2, p. 022109, 2002.

[23] A. Vutha, M. Horbatsch, and E. Hessels, "Orientation-dependent hyperfine structure of polar molecules in a rare-gas matrix: A scheme for measuring the electron electric dipole moment," *Phys. Rev. A*, vol. 98, no. 3, p. 032513, 2018.

[24] E. Tiesinga, P. J. Mohr, D. B. Newell, and B. N. Taylor, "Codata recommended values of the fundamental physical constants: 2018," *J.of Physical and Chemical Reference Data*, vol. 50, no. 3, p. 033105, 2021.

[25] Y. Ema, T. Gao, and M. Pospelov, "Standard model prediction for paramagnetic edms," *arXiv:2202.10524*, 2022.

[26] V. Dzuba and V. Flambaum, "Calculation of the (t, p)-odd electric dipole moment of thallium and cesium," *Phys. Rev. A*, vol. 80, no. 6, p. 062509, 2009.

[27] B. Graner, Y. Chen, E. Lindahl, B. Heckel, *et al.*, "Reduced limit on the permanent electric dipole moment of hg 199," *Phys. Rev. Lett.*, vol. 116, no. 16, p. 161601, 2016.

[28] Y. Ema, T. Gao, and M. Pospelov, "Improved indirect limits on muon electric dipole moment," *Phys. Rev. Lett.*, vol. 128, no. 13, p. 131803, 2022.

[29] Y. Ema, T. Gao, and M. Pospelov, "Reevaluation of heavy-fermion-induced electron edm at three loops," *arXiv:2207.01679*, 2022.

[30] G. Bennett, B. Bousquet, H. Brown, G. Bunce, R. Carey, P. Cushman, G. Danby, P. Debevec, M. Deile, H. Deng, *et al.*, "Improved limit on the muon electric dipole moment," *Phys. Rev. D*, vol. 80, no. 5, p. 052008, 2009.

[31] K. Inami, K. Hayasaka, I. Adachi, H. Aihara, S. Al Said, D. Asner, V. Aulchenko, T. Aushev, R. Ayad, V. Babu, *et al.*, "An improved search for the electric dipole moment of the τ lepton," *J.of High Energy Phys.*, vol. 2022, no. 4, pp. 1–17, 2022.

[32] Y. Ema, T. Gao, and M. Pospelov, "Improved indirect limits on charm and bottom quark edms," *arXiv:2205.11532*, 2022.

[33] W. Altmannshofer, J. Brod, and M. Schmaltz, "Experimental constraints on the coupling of the higgs boson to electrons," *J. of HE Phys.*, vol. 2015, no. 5, pp. 1–20, 2015.

[34] H. Bahl, E. Fuchs, S. Heinemeyer, J. Katzy, M. Menen, K. Peters, M. Saimpert, and G. Weiglein, "Constraining the cp structure of higgs-fermion couplings with a global lhc fit, the electron edm and baryogenesis," *The European Physical Journal C*, vol. 82, no. 7, pp. 1–30, 2022.

[35] J. B. Araujo, R. Casana, and M. M. Ferreira Jr, "Constraining c p t-even and lorentz-violating nonminimal couplings with the electron magnetic and electric dipole moments," *Phys. Rev. D*, vol. 92, no. 2, p. 025049, 2015.

[36] Z. Lasner, *Order-of-magnitude-tighter bound on the electron electric dipole moment.* PhD thesis, Yale University, 2019.

[37] D. Budker and M. G. Kozlov, "Sensing: equation one," *arXiv:2011.11043*, 2020.

[38] U. Dargyte, D. M. Lancaster, and J. D. Weinstein, "Optical and spin-coherence properties of rubidium atoms trapped in solid neon," *Phys. Rev. A*, vol. 104, no. 3, p. 032611, 2021.

[39] M. Browne, "Effects of applied electric fields on paramagnetic resonance in chrome alums," *Phys. Rev.*, vol. 121, no. 6, p. 1699, 1961.

[40] E. Royce and N. Bloembergen, "Linear electric shifts in the paramagnetic resonance of al 2 o 3: Cr and mgo: Cr," *Phy. Rev.*, vol. 131, no. 5, p. 1912, 1963.

[41] B. Vasil'Ev and E. Kolycheva, "Measurement of the electric dipole moment of the electron with a quantum interferometer," *Sov. Phys.-JETP (Engl. Transl.);(United States)*, vol. 47, no. 2, 1978.

[42] B. Heidenreich, O. Elliott, N. Charney, K. Virgien, A. Bridges, M. McKeon, S. Peck, D. Krause Jr, J. Gordon, L. Hunter, *et al.*, "Limit on the electron electric dipole moment in gadolinium-iron garnet," *Phys. Rev. Lett.*, vol. 95, no. 25, p. 253004, 2005.

[43] Y. Kim, C.-Y. Liu, S. Lamoreaux, G. Visser, B. Kunkler, A. Matlashov, J. Long, and T. Reddy, "New experimental limit on the electric dipole moment of the electron in a paramagnetic insulator," *Phys. Rev. D*, vol. 91, no. 10, p. 102004, 2015.

[44] S. Eckel, A. Sushkov, and S. Lamoreaux, "Limit on the electron electric dipole moment using paramagnetic ferroelectric eu 0.5 ba 0.5 tio 3," *Phys. Rev. Lett.*, vol. 109, no. 19, p. 193003, 2012.

[45] F. L. Shapiro, "Electric dipole moments of elementary particles.," tech. rep., Joint Inst. for Nuclear Research, Dubna, USSR, 1968.

[46] D. Budker, P. W. Graham, M. Ledbetter, S. Rajendran, and A. O. Sushkov, "Proposal for a cosmic axion spin precession experiment (casper)," *Phys. Rev. X*, vol. 4, no. 2, p. 021030, 2014.

[47] C. Pryor and F. Wilczek, ""artificial vacuum" for t-violation experiment," *Phys. Lett.B*, vol. 194, no. 1, pp. 137–140, 1987.

[48] M. Arndt, S. Kanorsky, A. Weis, and T. Hänsch, "Can paramagnetic atoms in superfluid helium be used to search for permanent electric dipole moments?," *Phys. Lett. A*, vol. 174, no. 4, pp. 298–303, 1993.

[49] M. Arndt, S. Kanorsky, A. Weis, and T. Hänsch, "Long electronic spin relaxation times of cs atoms in solid 4 he," *Phys. Rev. Lett.*, vol. 74, no. 8, p. 1359, 1995.

[50] P. Moroshkin, A. Hofer, and A. Weis, "Atomic and molecular defects in solid 4he," *Phys. Rep.*, vol. 469, no. 1, pp. 1–57, 2008.

[51] S. J. Li, R. Anderson, and A. C. Vutha, "Baf molecules trapped in neon ice," *arXiv:2207.07279*, 2022.

[52] C. Braggio, R. Calabrese, G. Carugno, G. Fiscelli, M. Guarise, A. Khanbekyan, A. Noto, R. Passante, L. Rizzuto, G. Ruoso, *et al.*, "Spectroscopy of alkali atoms in solid matrices of rare gases: Experimental results and theoretical analysis," *Applied Sciences*, vol. 12, no. 13, p. 6492, 2022.

[53] M. Grenzi, "Development of a new experimental setup for the measurement of electron electric dipole moment,"

[54] S. Kain and G. Gabrielse, "Measurement of the electron electric dipole moment using an ensemble of 183wc molecules dispersed in solid parahydrogen," *Bulletin of the American Physical Society*, 2020.

[55] H. Schmid, "Some symmetry aspects of ferroics and single phase multiferroics," *Journal of Physics.: Condensed Matter*, vol. 20, no. 43, p. 434201, 2008.

[56] A. Borovik-Romanov, H. Grimmer, and M. Kenzelmann, "Magnetic properties," 2013.

[57] J.-P. Rivera, "A short review of the magnetoelectric effect and related experimental techniques on single phase (multi-) ferroics," *The European Physical Journal B*, vol. 71, no. 3, pp. 299–313, 2009.

[58] W. Bialek, J. Moody, and F. Wilczek, "Macroscopic t nonconservation: Prospects for a new experiment," *Phys. Rev. Lett.*, vol. 56, no. 16, p. 1623, 1986.

[59] C.-Y. Liu and S. Lamoreaux, "A new search for a permanent dipole moment of the electron in a solid state system," *Modern Phys. Lett. A*, vol. 19, no. 13n16, pp. 1235–1238, 2004.

[60] A. Sushkov, S. Eckel, and S. Lamoreaux, "Prospects for a new search for the electron electric-dipole moment in solid gadolinium-iron-garnet ceramics," *Phys. Rev. A*, vol. 79, no. 2, p. 022118, 2009.

[61] G. K. Ozerov, D. S. Bezrukov, and A. A. Buchachenko, "Generic accommodations of an atom in the lennard-jones fcc and hcp rare-gas solids: A computational study," *Phys. Rev. B*, vol. 103, no. 18, p. 184110, 2021.

[62] L. Blank, D. E. Weeks, and G. S. Kedziora, "M+ ng potential energy curves including spin-orbit coupling for m= k, rb, cs and ng= he, ne, ar," *J. Chem. Phys.*, vol. 136, no. 12, p. 124315, 2012.

[63] E. Ascher, "Higher-order magneto-electric effects," *The Philosophical Magazine*, vol. 17, no. 145, pp. 149–157, 1968.

[64] P. Pathak, *Absorption spectrum of rubidium in a solid neon matrix.* PhD thesis, 2014.

[65] S. K. Regmi, *Optical pumping of rubidium spin in a solid argon matrix.* PhD thesis, 2013.

[66] R. Swanepoel, "Determination of the thickness and optical constants of amorphous silicon," *J.of Phys. E: Scientific Instruments*, vol. 16, no. 12, p. 1214, 1983.

[67] A. Sinnock and B. Smith, "Refractive indices of the condensed inert gases," *Phys. Rev.*, vol. 181, no. 3, p. 1297, 1969.

[68] S. L. Kupferman and F. Pipkin, "Properties of rubidium atoms trapped in a solid argon matrix," *Phys. Rev.*, vol. 166, no. 2, p. 207, 1968.

[69] I. Gerhardt, K. Sin, and T. Momose, "Excitation and emission spectra of rubidium in rare-gas thin-films," *J.of Chem. Phys.*, vol. 137, no. 1, p. 014507, 2012.

[70] C. Hartzell, *Matrix Isolation of Rubidium in a Solid Para-Hydrogen Substrate - BS Thesis, University of Nevada, Reno.* 2014.

[71] R. Massey, T. Kitching, and J. Richard, "The dark matter of gravitational lensing," *Reports on Progress in Phys.*, vol. 73, no. 8, p. 086901, 2010.

[72] R. D. Peccei and H. R. Quinn, "CP conservation in the presence of pseudoparticles," *Phys. Rev. Lett.*, vol. 38, pp. 1440–1443, Jun 1977.

[73] S. Weinberg, "A new light boson?," *Phys. Rev. Lett.*, vol. 40, pp. 223–226, Jan 1978.

[74] F. Wilczek, "Problem of strong p and t invariance in the presence of instantons," *Phys. Rev. Lett.*, vol. 40, pp. 279–282, Jan 1978.

[75] M. Gorghetto and G. Villadoro, "Topological susceptibility and qcd axion mass: Qed and nnlo corrections," *J.of High Energy Phys.*, vol. 2019, no. 3, pp. 1–22, 2019.

[76] L. Di Luzio, M. Giannotti, E. Nardi, and L. Visinelli, "The landscape of qcd axion models," *Phys. Reports*, vol. 870, pp. 1–117, 2020.

[77] P. Sikivie, "Invisible axion search methods," *Reviews of Modern Phys.*, vol. 93, no. 1, p. 015004, 2021.

[78] J. et al., "Axion dark matter," *arXiv e-prints*, pp. arXiv–2203, 2022.

[79] A. Ringwald, "Searching for axions and alps from string theory," in *J.of Phys.: Conference Series*, vol. 485, p. 012013, IOP Publishing, 2014.

[80] D. Budker, V. V. Flambaum, X. Liang, and A. Zhitnitsky, "Axion quark nuggets and how a global network can discover them," *Phys. Rev. D*, vol. 101, no. 4, p. 043012, 2020.

[81] V. Domcke, Y. Ema, K. Mukaida, and M. Yamada, "Spontaneous baryogenesis from axions with generic couplings," *J.of High Energy Phys.*, vol. 2020, no. 8, pp. 1–49, 2020.

[82] Y. Stadnik, V. Dzuba, and V. Flambaum, "Improved limits on axionlike-particle-mediated p, t-violating interactions between electrons and nucleons from electric dipole moments of atoms and molecules," *Phys. Rev. Lett.*, vol. 120, no. 1, p. 013202, 2018.

[83] P. Sikivie and Q. Yang, "Bose-einstein condensation of dark matter axions," *Phys. Rev. Lett.*, vol. 103, no. 11, p. 111301, 2009.

[84] D. J. Marsh, "Axion cosmology," *Phys. Reports*, vol. 643, pp. 1–79, 2016.

[85] Y. Stadnik and V. Flambaum, "Axion-induced effects in atoms, molecules, and nuclei: Parity nonconservation, anapole moments, electric dipole moments, and spin-gravity and spin-axion momentum couplings," *Phys. Rev. D*, vol. 89, no. 4, p. 043522, 2014.

[86] J. E. Kim and G. Carosi, "Axions and the strong cp problem," *Reviews of Modern Phys.*, vol. 82, no. 1, p. 557, 2010.

[87] C. Hogan and M. Rees, "Axion miniclusters," *Phys. Lett. B*, vol. 205, no. 2-3, pp. 228–230, 1988.

[88] B. Holdom, "Domain walls. i. axion models," *Phys. Rev. D*, vol. 27, no. 2, p. 332, 1983.

[89] Y. Stadnik and V. Flambaum, "Searching for topological defect dark matter via nongravitational signatures," *Phys. Rev. Lett.*, vol. 113, no. 15, p. 151301, 2014.

[90] T. S. Roussy, D. A. Palken, W. B. Cairncross, B. M. Brubaker, D. N. Gresh, M. Grau, K. C. Cossel, K. B. Ng, Y. Shagam, Y. Zhou, *et al.*, "Experimental constraint on axionlike particles over seven orders of magnitude in mass," *Phys. Rev. Lett.*, vol. 126, no. 17, p. 171301, 2021.

[91] S. Pustelny, D. F. Jackson Kimball, C. Pankow, M. P. Ledbetter, P. Wlodarczyk, P. Wcislo, M. Pospelov, J. R. Smith, J. Read, W. Gawlik, *et al.*, "The global network of optical magnetometers for exotic physics (gnome): A novel scheme to search for physics beyond the standard model," *Annalen der Physik*, vol. 525, no. 8-9, pp. 659–670, 2013.

[92] H. Czyz, K. Kołodziej, M. Zrałek, and P. Christova, "Is the anapole moment a physical observable?," *Canadian J.of Phys.*, vol. 66, no. 2, pp. 132–134, 1988.

[93] A. Góngora-T and R. G. Stuart, "The charge radius and anapole moment of a free fermion," *Zeitschrift für Physik C Particles and Fields*, vol. 55, no. 1, pp. 101–105, 1992.

[94] C. Wood, S. Bennett, D. Cho, B. Masterson, J. Roberts, C. Tanner, and C. E. Wieman, "Measurement of parity nonconservation and an anapole moment in cesium," *Science*, vol. 275, no. 5307, pp. 1759–1763, 1997.

[95] B. Roberts, V. Dzuba, and V. Flambaum, "Parity and time-reversal violation in atomic systems," *Annual Review of Nuclear and Particle Science*, vol. 65, no. 1, pp. 63–86, 2015.

[96] H. Tan and A. Derevianko, "Implications of w-boson mass for atomic parity violation," *arXiv:2204.11991*, 2022.

[97] CDF Collaboration, T. Aaltonen, S. Amerio, D. Amidei, A. Anastassov, A. Annovi, J. Antos, G. Apollinari, J. Appel, T. Arisawa, *et al.*, "High-precision measurement of the w boson mass with the cdf ii detector," *Science*, vol. 376, no. 6589, pp. 170–176, 2022.

[98] K. Kumar, S. Mantry, W. Marciano, and P. Souder, "Low energy measurements of the weak mixing angle," *arXiv:1302.6263*, 2013.

[99] M. Safronova, D. Budker, D. DeMille, D. F. J. Kimball, A. Derevianko, and C. W. Clark, "Search for new physics with atoms and molecules," *Reviews of Modern Phys.*, vol. 90, no. 2, p. 025008, 2018.

[100] E. Radescu and G. Vaman, "Exact calculation of the angular momentum loss, recoil force, and radiation intensity for an arbitrary source in terms of electric, magnetic, and toroid multipoles," *Phys. Rev. E*, vol. 65, no. 4, p. 046609, 2002.

[101] N. Talebi, S. Guo, and P. A. van Aken, "Theory and applications of toroidal moments in electrodynamics: their emergence, characteristics, and technological relevance," *Nanophotonics*, vol. 7, no. 1, pp. 93–110, 2018.

[102] W. Haxton, E. Henley, and M. Musolf, "Nucleon and nuclear anapole moments," *Phys. Rev. Lett.*, vol. 63, no. 9, p. 949, 1989.

[103] V. Flambaum and I. Khriplovich, "P-odd nuclear forces: a source of parity violation in atoms," *Sov. Phys.-JETP (Engl. Transl.);(United States)*, vol. 52, no. 5, 1980.

[104] B. Roberts, V. Dzuba, and V. Flambaum, "Parity and time-reversal violation in atomic systems," *arXiv:1412.6644*, 2014.

[105] W. Johnson, M. Safronova, and U. Safronova, "Combined effect of coherent z exchange and the hyperfine interaction in the atomic parity-nonconserving interaction," *Phys. Rev. A*, vol. 67, no. 6, p. 062106, 2003.

[106] D. DeMille, S. B. Cahn, D. Murphree, D. A. Rahmlow, and M. G. Kozlov, "Using molecules to measure nuclear spin-dependent parity violation," *Phys. Rev. Lett.*, vol. 100, no. 2, p. 023003, 2008.

[107] D. Sheng, L. Orozco, and E. Gomez, "Preliminary studies for anapole moment measurements in rubidium and francium," *J.of Phys. B: Atomic, Molecular and Optical Phys.*, vol. 43, no. 7, p. 074004, 2010.

[108] I. B. Khriplovich, "Parity nonconservation in atomic phenomena," 1991.

[109] J. Guéna, M. Lintz, and M.-A. Bouchiat, "Atomic parity violation: Principles, recent results, present motivations," *Modern Phys. Lett. A*, vol. 20, no. 06, pp. 375–389, 2005.

[110] M. Kozlov, S. Porsev, and W. Johnson, "Parity nonconservation in thallium," *Phys. Rev. A*, vol. 64, no. 5, p. 052107, 2001.

[111] M.-A. Bouchiat and C. Bouchiat, "An atomic linear stark shift violating p but not t arising from the electroweak nuclear anapole moment," *The European Physical Journal D*, vol. 15, no. 1, pp. 5–18, 2001.

[112] C. Bouchiat and C. Piketty, "Nuclear spin dependent atomic parity violation, nuclear anapole moments and the hadronic axial neutral current," *Zeitschrift für Physik C Particles and Fields*, vol. 49, no. 1, pp. 91–107, 1991.

[113] V. Ezhov, M. Kozlov, G. Krygin, V. Ryzhov, and V. Ryabov, "On the possibility of measuring the anapole moment of potassium atom," *Technical Phys. Lett.*, vol. 30, no. 11, pp. 917–919, 2004.

[114] B. Mong, S. Cook, T. Walton, C. Chambers, A. Craycraft, C. Benitez-Medina, K. Hall, W. Fairbank Jr, J. Albert, D. Auty, *et al.*, "Spectroscopy of ba and ba+ deposits in solid xenon for barium tagging in nexo," *Phys. Rev. A*, vol. 91, no. 2, p. 022505, 2015.

[115] V. Dzuba and V. Flambaum, "Current trends in searches for new physics using measurements of parity violation and electric dipole moments in atoms and molecules," *arXiv:1009.4960*, 2010.

[116] T. Mukhamedjanov, O. Sushkov, and J. Cadogan, "Manifestations of nuclear anapole moments in solid-state nmr," *Phys. Rev. A*, vol. 71, no. 1, p. 012107, 2005.

[117] Y. Stadnik and V. Flambaum, "Improved limits on standard model extension parameters and applications to axion dark matter searches," *arXiv:1408.2184*, 2014.

[118] V. Dmitriev, I. Khriplovich, and V. Telitsin, "Nuclear anapole moments in single-particle approximation," *Nuclear Phys. A*, vol. 577, no. 3-4, pp. 691–708, 1994.